



Mitigating off-target distribution and enhancing cytotoxicity in breast cancer cells with alpha-ketoglutaric acid-modified Fe/Mg-CA nanoparticles

Sheikh Tanzina Haque¹ · Md. Emranul Karim¹ · Iekhsan Othman¹ · Ezharul Hoque Chowdhury^{1,2}

Received: 11 January 2022 / Accepted: 16 March 2022 / Published online: 5 April 2022
© The Author(s) 2022

Abstract

Purpose In this work, pH-sensitive alpha-ketoglutaric acid-modified Fe/Mg-carbonate apatite (α -KAM-Fe/Mg-CA) NPs were introduced and found to be capable of promoting the selective delivery of cancer-killing drug doxorubicin (DOX) in breast cancer cells, while simultaneously mitigating DOX toxicity on normal cells.

Methods As part of the characterization and evaluation of α -KAM-Fe/Mg-CA NPs to target breast cancer cells, a series of assessments were performed, which included size measurements, morphological analysis, FTIR, cytotoxicity assessment, hemolysis, drug binding, cellular uptake, and pH-responsive drug release tests. Liquid chromatography-mass spectrometry was used to conduct the protein corona analysis of α -KAM-Fe/Mg-CA using 10% FBS (fetal bovine serum) and mice plasma. Furthermore, to investigate the distribution of DOX-loaded α -KAM-Fe/Mg-CA NPs in major tissues and the tumor, a biodistribution investigation was conducted in mammary tumor-induced Balb/c mouse models 24 h after the intravenous administration of DOX-loaded α -KAM-Fe/Mg-CA NPs.

Results The in vitro pH-dependent release of DOX over time demonstrated that α -KAM-Fe/Mg-CA NPs were pH-responsive and degraded rapidly at acidic pH levels. When compared to free DOX, the DOX-loaded α -KAM-Fe/Mg-CA NPs demonstrated a potent antiproliferative effect on breast cancer cells. Confocal microscopy confirmed the effective internalization of DOX-loaded α -KAM-Fe/Mg-CA NPs in breast cancer cells. The protein corona analysis revealed an affinity for dysopsonins (serum albumin, apolipoproteins) and transport proteins that may assist in extending their blood circulation period. Furthermore, biodistribution data of DOX-loaded α -KAM-Fe/Mg-CA NPs in the mammary tumor-induced Balb/c mouse model indicated extended circulation in the bloodstream, reduced non-target distribution in major tissues, and increased drug accumulation in the tumor.

Conclusion The results obtained suggest that α -KAM-Fe/Mg-CA NPs may emerge as a prospective candidate for delivering therapeutic cargos to treat malignant mammary tumors.

Keywords Inorganic nanoparticles · Breast cancer · pH-responsive drug release · Alpha-ketoglutaric acid-modified Fe/Mg-carbonate apatite (α -KAM-Fe/Mg-CA) · Protein corona · Biodistribution

✉ Ezharul Hoque Chowdhury
md.ezharul.hoque@monash.edu

Sheikh Tanzina Haque
sheikh.haque@monash.edu

Md. Emranul Karim
karim604306@gmail.com

Iekhsan Othman
iekhsan.othman@monash.edu

¹ Jeffrey Cheah School of Medicine and Health Sciences, Monash University Malaysia, Jalan Lagoon Selatan, Bandar Sunway, 47500 Subang Jaya, Selangor, Malaysia

² Health and Wellbeing Cluster, Global Asia in the 21st Century (GA21) Platform, Jeffrey Cheah School of Medicine and Health Sciences, Monash University Malaysia, Jalan Lagoon Selatan, Bandar Sunway, 47500 Subang Jaya, Selangor, Malaysia

Introduction

Cancer cells, including breast cancer cells, are commonly treated with surgical intervention, radiation therapy, adjuvant and neoadjuvant chemotherapy, immunotherapy, or combination therapy. For metastatic cancer, surgical tumor excisions accompanied by chemotherapy are often prescribed to achieve therapeutic effects (Xu et al. 2015). However, due to the non-selective nature of chemotherapy drugs to localize in both healthy and cancerous cells, adverse effects such as cardiotoxicity, hair loss, nausea, kidney failure, neuropathy, tissue damage, and inflammation are often observed (Tian et al. 2017; Senapati et al. 2018). Moreover, the toxicity in healthy tissues restricts the dose and frequency of chemotherapeutics, which may potentially lead to multidrug resistance (MDR) (Dong et al. 2010; Qi et al. 2017; Senapati et al. 2018), attributable to the over-expression of p-glycoprotein membrane transporters (Nakamura et al. 2016; ud Din et al. 2017; Xin et al. 2017). As a broad-spectrum drug, DOX is widely recommended for first-line chemotherapy (Hortobagyi 1997) to treat various cancers, including breast cancer. DOX exerts toxicity by intercalating the DNA, generating free radicals, and inhibiting the topoisomerase II enzymes, thus preventing cell division and inducing apoptosis in the invasive cancer cells. However, treatment with DOX raises serious concerns due to its non-selective action in healthy cells, thus leading to adverse effects such as cardiomyopathy, leukemia, nausea, and vomiting (Carvalho et al. 2009; Peetla et al. 2010). Secondly, DOX can be rapidly pumped out of the cancer cells after being passively internalized due to MDR, thus compromising its therapeutic efficacy in cancer treatment. Incorporating DOX into nano-carriers could effectively avoid the unwanted toxicity associated with the free drugs.

Given the need to address the challenges imposed by free anticancer drugs, nanoparticle (NP)-based drug delivery platforms have been exploited extensively over the last couple of decades (Wicki et al. 2015). These nano-carriers are bigger than small molecule drugs, thereby prolonging the blood circulation period and promoting the accumulation of encapsulated drugs in the tumor (Li et al. 2016) by restricting their renal clearance and broad tissue distribution, as well as harnessing the enhanced permeability and retention (EPR) effect of the porous vasculatures and underdeveloped lymphatic system of the tumor (Li et al. 2009). In addition, NPs are considered to bypass MDR (Qi et al. 2017) and possess the potential ability of controlled drug release (ud Din et al. 2017; Ventola 2017). With growing evidence, different NPs-based drug delivery platforms such as liposomes and polymeric micelles (Rivera 2003; Panchapakesan et al. 2005; Shao et al. 2007; Kumari

et al. 2010) have captured significant attention for their potential in preventing and treating cancer. Additionally, the therapeutic potential of inorganic NPs has been widely explored with respect to their unique properties, including tunable morphology and size, large surface area to volume ratio, elasticity, biocompatibility, stability, porosity, and inertness (Shi et al. 2017; Haque et al. 2018). A common approach to generating bio-functional inorganic NPs is to coat their surface with suitable hydrophilic macromolecules, thereby manipulating their physicochemical properties to enhance the targeted delivery and therapeutic efficacy of a therapeutic molecule, while overcoming the impediments associated with the use of inorganic NPs (Haque et al. 2018).

Stimulus responsive approaches, such as those based on pH, temperature, enzymes, light, magnetic and electric fields, are widely adopted. These could selectively enhance the controlled delivery of drug cargos to the targeted cancer site, and thus alleviate the side effects of chemotherapy (Cui et al. 2017; Oshiro-Junior et al. 2018). In particular, pH-responsive nano-carriers can potentiate the therapeutic efficacy of drugs. Due to their sensitivity towards acidic pH levels, they disintegrate in the extracellular milieu (pH 6.5–6.8) of the tumor microenvironment or within the endosome (pH 5.5–6) or lysosome (pH 4.5–5) of cancer cells (Prasad et al. 2020), while remaining stable in blood and extracellular fluid of normal tissues (pH 7.4). Thus, biological toxicity is reduced due to off-target distribution. Furthermore, the targeted delivery of therapeutic payloads in cancer cells through active or passive targeting is fostered (Cho et al. 2008; Gao et al. 2010; Bae et al. 2011; Hatakeyama, 2017). In active targeting, the ligands present on the nano-carriers bind with the receptor-positive cancer cells, improving the uptake of drugs in cancer cells (Attia et al. 2019). In passive targeting, drug-conjugated nano-carriers (200–800 nm) not only pass through the leaky vasculatures of the cancer tissues but also remain there, due to the poorly developed lymphatic drainage as a result of EPR effect (Peer et al. 2007; Attia et al. 2019). However, existing pH-sensitive nano-carriers such as liposomes (Torchilin, 2005), polymeric micelles (Wu et al. 2013), hydrogel (Abandansari et al. 2014) often suffer from a variety of limitations, including poor scalability, premature drug degradation, reduced blood circulation period, ineffective drug release, slow biodegradation, and instability (Haque et al. 2020a, b). Among a myriad of inorganic NPs, pH-sensitive carbonate apatite (CA), $\text{Ca}_{10}(\text{PO}_4)_{6-x}(\text{CO}_3)_x(\text{OH})_2$ has stirred up significant interest due to its versatile characteristics, including biocompatibility, heterogeneous charge distribution, tunable size and shape, and ability to passively accumulate in the tumor through EPR effect and dissociate completely in the endosomal pH, leading to the effective release of

therapeutics into the cytosol of the cancer cells (Chowdhury 2007, 2013; Chowdhury et al. 2006).

Alpha ketoglutaric acid (α -KA) (2-ketoglutaric acid or 2-oxoglutaric acid) is a non-toxic, highly water-soluble, low molecular weight endogenous metabolite of the Krebs cycle (Filip et al. 2007). Besides, α -KA can suppress angiogenesis (Donnarumma et al. 2013). Most α -KA is produced in the Krebs cycle, where it undergoes oxidative decarboxylation by α -ketoglutarate dehydrogenase. The two carboxyl groups present at opposite ends of the carbon backbone stimulate its acidic characteristics, whereas the ketone domain modulates its reactivity. In our previous report, fabrication of CA with α -KA showed reduced particle size and improved drug build-up in the tumor (Hossain et al. 2019; Hossain et al. 2020). Another study in our lab revealed that modification of CA with Fe and Mg led to a successful reduction in the aggregation associated with CA, with improved drug binding efficacy and enhanced cytotoxicity in breast cancer cells (Haque et al. 2020a, b).

Considering the advantages of α -KA and Fe/Mg-CA, this paper reports on the modification of Fe/Mg-CA with α -KA (α -KAM-Fe/Mg-CA) to ensure the pH-responsive controlled release, prolonged plasma half-life, and selective delivery of DOX in breast carcinoma. DOX-loaded α -KAM-Fe/Mg-CA NPs were evaluated in terms of their biocompatibility, loading efficiency, cellular internalization, and antiproliferative effects on MCF-7 cells. Protein corona analysis by LCMS was conducted with mice plasma and 10% FBS (Fetal Bovine Serum) to investigate the ex vivo interaction of the serum proteins with the NPs. The biodistribution study and blood plasma analysis were performed on 4T1 (murine breast tumor cell line)-induced mammary tumor-bearing Balb/c mice to determine the blood circulation time and biodistribution patterns of DOX.

Materials and methods

Materials

Ferric chloride hexahydrate ($\text{FeCl}_3 \cdot 6\text{H}_2\text{O}$), magnesium chloride hexahydrate ($\text{MgCl}_2 \cdot 6\text{H}_2\text{O}$), alpha-ketoglutaric acid disodium salt hydrate (α -KA), calcium chloride dihydrate ($\text{CaCl}_2 \cdot 2\text{H}_2\text{O}$), Dulbecco's modified eagle medium (DMEM), sodium bicarbonate (NaHCO_3), thiazolyl blue tetrazolium bromide (MTT), doxorubicin hydrochloride (DOX), dimethyl sulphoxide (DMSO), and ethylenediamine tetraacetic acid (EDTA) were acquired from Sigma-Aldrich (St. Louis, MO, USA). DMEM powder, penicillin–streptomycin, trypsin–ethylene diamine tetraacetate (trypsin–EDTA), and fetal bovine serum (FBS) were purchased from Gibco by Life Technology (Thermo Fischer Scientific, Waltham, MA, USA). Hydrochloric acid (HCl)

and ethanol were obtained from Fischer Scientific (Loughborough, Leicestershire, UK). MCF-7 (Michigan Cancer Foundation-7) and 4T1 (mouse mammary tumor) cells were procured from ATCC (Manassas, Virginia, USA).

Effect of α -KA on the growth of Fe/Mg-CA NPs based on measurements of absorbance and optical imaging

To fabricate and optimize α -KAM-Fe/Mg-CA and α -KAM-CA NPs, five different concentrations of α -KA disodium salt hydrates (i.e., 2 mM, 4 mM, 6 mM, 8 mM, and 10 mM) were added independently for formulating Fe/Mg-CA along with 4 mM Ca^{2+} , 5 μM Fe^{3+} and 12 mM Mg^{2+} , and CA along with 4 mM Ca^{2+} in bicarbonated DMEM media. Then, the mixtures were incubated at 37 °C for 30 min. Each sample was supplemented with 10% FBS. The turbidity of each formulation was determined at 320 nm with an 1800 MS UV–VIS spectrophotometer (Shimadzu Scientific Instruments Inc.).

The turbidity of α -KA in DMEM was separately measured to determine if the salt interfered with the turbidity of α -KAM-Fe/Mg-CA and α -KAM-CA NPs. The absorbance was evaluated as mean value \pm standard deviation for each of the samples, which were prepared in triplicate.

The dispersion and agglomeration of the α -KAM-CA and α -KAM-Fe/Mg-CA NPs prepared with different concentrations of α -KA (i.e., 2 mM, 4 mM, 6 mM, 8 mM, and 10 mM) were captured after incubation for 30 min by an Olympus IX81 fluorescence microscope (Shinjuku, Tokyo, Japan). The optical microscopic images were immediately acquired after placing the samples into a 24-well plate, with a scale bar: 50 μm at a magnification 10 \times .

Zeta (Z) average diameter and surface potential measurement of α -KAM-Fe/Mg-CA NPs

Fe/Mg-CA and CA NPs were fabricated in the presence of elevated concentrations of α -KA (i.e., 2 mM, 4 mM, 6 mM, 8 mM, and 10 mM). The z-average diameter of the respective NPs was evaluated utilizing a Malvern nano zeta sizing device (Malvern, Worcestershire, UK). The z-average diameter was measured employing dynamic light scattering (DLS). Each sample was prepared in duplicate. The z-average diameter and the surface charge (zeta potential) were calculated using mean value and standard deviation values (Hossain et al. 2018).

The average size of the diluted samples of α -KAM-CA (4 mM Ca^{2+} , 50 mM α -KA) and α -KAM-Fe/Mg-CA (4 mM Ca^{2+} , 5 μM Fe^{3+} , 12 mM Mg^{2+} and 50 mM α -KA) NPs were measured to analyze the effects of dilution (5, 10, 20, and 50-fold) of the original suspension prepared with high

concentrations of α -KA (50 mM) on the average size, both in the presence and absence of 10% FBS.

Field emission scanning electron microscope (FESEM) image analysis for α -KAM-Fe/Mg-CA NPs

The size, shape, and surface roughness of α -KAM-Fe/Mg-CA and α -KAM-CA NPs were visualized through FESEM (Hitachi/SU8010, Tokyo, Japan). The prepared samples of α -KAM-Fe/Mg-CA (4 mM Ca^{2+} , 5 μM Fe^{3+} , 12 mM Mg^{2+} , and 4 mM α -KA) and α -KAM-CA (4 mM Ca^{2+} , and 4 mM α -KA) were centrifuged at 13,000 rpm for 20 min and rinsed with Milli Q water. 2 μL suspension of α -KAM-Fe/Mg-CA and α -KAM-CA NPs were dried on a glass slide for 60 min. A sputter coater was then used to coat the samples with Pt (Platinum) for 40 s at 30 mA sputter current and 2.30 tooling factor following their placement on a carbon-coated sample holder. At a voltage of 2 kV, FESEM micrographs of the respective samples were captured (Hossain et al. 2018; Karim et al. 2019; Haque et al. 2020a, b).

Characterization of α -KAM-Fe/Mg-CA NPs by fourier transform infrared (FTIR) spectroscopy

On a Varian 640-IR, FTIR analysis was carried out at a wavelength of 4000–400 cm^{-1} . The data analysis was conducted using Varian Resolution Pro 640 software (Agilent, Santa Clara, CA, USA) at a resolution of 4 cm^{-1} . After inducing the formation of α -KAM-Fe/Mg-CA (40 mM Ca^{2+} , 50 μM Fe^{3+} , 120 mM Mg^{2+} , and 40 mM α -KA) and α -KAM-CA (40 mM Ca^{2+} and 40 mM α -KA) at 37 °C for 30 min, samples were subjected to centrifugation (3200 rpm, 30 min). Following decantation of the supernatants, the pellets were washed and centrifuged. The precipitated pellets were freeze-dried (Labconco, Kansas City, MO, USA) after being refrigerated at -20 °C for 30 min to determine the IR spectra of the samples.

Effects of acidic pHs on dissolution of α -KAM-Fe/Mg-CA NPs

The α -KAM-Fe/Mg-CA (20 mM Ca^{2+} , 25 μM Fe^{3+} , 60 mM Mg^{2+} , and 20 mM α -KA) and α -KAM-CA (20 mM Ca^{2+} and 20 mM α -KA) NPs were prepared in 200 μL bicarbonated DMEM through 30 min incubation at 37 °C. Subsequently, 800 μL bicarbonated DMEM of various pHs (i.e., 7.5, 7, 6.5, 6, and 5.5) were added separately to the mixtures. Finally, the absorbance of the mixtures was assessed at 320 nm wavelength using an 1800 MS UV–VIS spectrophotometer (Shimadzu Scientific Instruments Inc.). The turbidity of each sample, prepared in triplicate, was assessed using the mean value and standard deviation.

pH-responsive DOX release from DOX-loaded α -KAM-Fe/Mg-CA NPs

In this study, 800 μL DMEM of various pHs (7.5, 7, 6.5, 6, and 5.5) were added to DOX-loaded α -KAM-Fe/Mg-CA NPs (20 mM Ca^{2+} , 25 μM Fe^{3+} , 60 mM Mg^{2+} , 20 mM α -KA, and 5 μM DOX) as well as DOX-loaded α -KAM-CA NPs (20 mM Ca^{2+} , 20 mM α -KA, and 5 μM DOX), which were initially prepared in 200 μL bicarbonated DMEM through incubation at 37 °C (30 min). Each sample was centrifuged at 12,000 rpm (20 min, 4 °C). After discarding the supernatant of the samples, the pellets were dissolved in 10 mM EDTA in PBS (EDTA solution prepared in phosphate buffer saline) in order to allow the bound drugs to be released from the NPs. The fluorescence intensity of DOX released from the respective NPs was then measured over time (0, 30, 60, 90 and 120 min) using the 2030 multilabel reader Victor X5 with the 2030 manager software from PerkinElmer (Waltham, MA, USA) at an excitation (485 nm)/emission (535 nm) spectrum (Hossain et al. 2018). The standard curve and the formula mentioned below were used to estimate the release percentage (%) of DOX from DOX-loaded α -KAM-Fe/Mg-CA and DOX-loaded α -KAM-CA NPs.

$$\text{DOX Released (\%)} = \frac{\text{NPs bound DOX at pH7.5} - \text{NPs bound DOX at different pH(i.e., 7.5, 7, 6.5, 6, 5.5)}}{\text{NPs bound DOX at different pH(i.e., 7.5, 7, 6.5, 6, 5.5)}} \times 100$$

Stability analysis of α -KAM-Fe/Mg-CA NPs

The turbidity of α -KAM-CA and α -KAM-Fe/Mg-CA NPs was evaluated at 0 h, 4 h, 24 h, and 72 h through an 1800 MS UV–VIS spectrophotometer (Shimadzu, Japan) at 320 nm wavelength. The turbidity of the samples was assessed as mean value and standard deviation in triplicate (Hossain et al. 2019).

The data (in triplicate) of each sample was interpreted as mean \pm standard deviation.

DOX binding affinity for α -KAM-Fe/Mg-CA NPs

DOX (1, 2.5, 5, 7.5 and 10 μM) was added in increasing concentrations to DOX- α -KAM-Fe/Mg-CA and DOX- α -KAM-CA NPs. The samples were prepared in 1 mL bicarbonated DMEM (pH 7.5) by incubating for 30 min at 37 °C.

Centrifuging (20 min, 4 °C) was carried out at 12,000 rpm for the samples. The supernatants were decanted, and the pellets were dissolved in 10 mM EDTA in PBS. The samples' fluorescence intensity was determined at an excitation (485 nm)/emission (535 nm) spectrum utilizing a 2030 multilabel reader victor X5 (Hossain et al. 2018; Karim et al. 2019). The data were evaluated using the PerkinElmer 2030 manager software (PerkinElmer, Waltham, MA, USA).

Plotting of the fluorescence intensity versus the free DOX concentration generated the standard curve. The binding affinity of DOX to α -KAM-CA and α -KAM-Fe/Mg-CA NPs was calculated from the standard curve, using the following formula –

$$\text{Binding (\%)} \text{ of DOX with NPs} = \frac{\text{Free DOX Concentration (i.e., 1, 2.5, 5, 7.5, 10}\mu\text{M)}}{\text{Concentration of DOX (i.e., 1, 2.5, 5, 7.5, 10}\mu\text{M) loaded NPs}} \times 100$$

The data (in triplicate) of each sample was interpreted as mean \pm standard deviation.

Qualitative and quantitative cellular internalization of DOX- α -KAM-Fe/Mg-CA NPs

The cellular uptake of DOX-loaded α -KAM-Fe/Mg-CA and DOX-loaded α -KAM-CA NPs was performed using an Olympus fluorescence microscope IX81 (Shinjuku, Tokyo, Japan) and CellSens Dimension software. First, MCF-7 cells in the exponential growth phase were seeded (5×10^4 cells/well) in 24-well plates 24 h before treatment. The wells were then treated with free DOX (5 μ M DOX), DOX- α -KAM-Fe/Mg-CA, and DOX- α -KAM-CA in the presence of 10% FBS. After 4 h of treatment, the supernatant from the growth media was decanted, and the cells were rinsed once with EDTA in PBS (10 mM, 100 μ L) and twice with 100 μ L PBS. The fluorescent images were then captured using the Olympus Fluorescence microscope IX81 (Karim et al. 2019).

In order to quantify the data, the PBS was removed from the wells after the fluorescent images were taken and lysis was performed using a lysis buffer. Next, the fluorescence intensity for the internalized drug was determined at excitation (485 nm) and emission (535 nm) wavelengths with a 2030 multilabel reader victor X5 (PerkinElmer, Waltham, MA, USA) in conjunction with the PerkinElmer 2030 manager software (Hossain et al. 2018). Calculation of the NPs' cellular uptake was performed 4 h following treatment based on the standard curve and the formula below:

$$\text{Cellular Uptake (\%)} = \frac{\text{Fluorescence Intensity}_{\text{Internalized Drug}}}{\text{Fluorescence Intensity}_{\text{Free Drug}}} \times 100$$

The fluorescence intensity of the samples was assessed as mean value and standard deviation in triplicate.

Visualization of intracellular uptake of DOX-loaded α -KAM-Fe/Mg-CA NPs through confocal laser scanning microscope (CLSM)

The intracellular uptake and distribution of DOX-loaded α -KAM-Fe/Mg-CA and DOX-loaded α -KAM-CA NPs in MCF-7 cells were imaged through confocal microscopy. The seeding density of MCF-7 cells in glass coverslips of 4-well plates confocal chamber was 5×10^4 cells/well. After 48 h, the cells were treated with DOX-loaded α -KAM-Fe/Mg-CA, DOX-loaded α -KAM-CA, and free DOX. 10 μ g mL⁻¹ DOX was used for each sample. The culture media were removed after 4 h (37 °C, 5% CO₂) followed by two PBS washes. After

fixation with 4% paraformaldehyde at room temperature for 10 min (in the dark), the cells were washed in PBS (Wang et al. 2017; Lu et al. 2018). The cells were later stained with DAPI in PBS (DAPI:PBS = 1:1000) for 15 min and rinsed again with PBS (Lu et al. 2018). Finally, the slides were viewed under a CLSM (Nikon Instruments, Tokyo, Japan).

Evaluation of toxicity via MTT (3–4, 5-dimethylthiazol-2-yl-2, 5-diphenyltetrazolium bromide) assay

DOX-loaded α -KAM-Fe/Mg-CA and DOX-loaded α -KAM-CA NPs were fabricated with increasing concentrations of DOX (i.e., 1 nM, 10 nM, 100 nM, and 1 μ M) in 1 mL bicarbonated DMEM (pH 7.4), via 30 min of incubation at 37 °C and addition of 10% FBS. Free DOX samples were prepared by adding different concentrations (i.e., 1 nM, 10 nM, 100 nM, and 1 μ M) of DOX to DMEM. Then, incubation was carried out and 10% FBS was applied. The α -KAM-Fe/Mg-CA and α -KAM-CA NPs were generated in DMEM with 10% FBS added after 30 min of incubation at 37 °C.

After 24 h of seeding, the cells in each well were treated with the prepared NPs and incubated for 48 h at 37 °C (5% CO₂). Next, 50 μ L of MTT (5 mg/mL in PBS) solution was added to each well, and the incubation was conducted at 37 °C for 4 h. After 4 h, the supernatant from each well was aspirated. For the dissolution of the formazan crystals, 300 μ L of DMSO solution was used. The absorbance of the samples was evaluated through a microplate reader (BIO-RAD-Microplate Reader, Hercules, CA, USA) at an optical (595 nm)/reference (630 nm) wavelength (Hossain et al. 2018; Karim et al. 2019). The data (in triplicate) of each sample was interpreted as mean \pm standard deviation. The following formula was used to estimate the cell viability (%):

$$\text{Cell Viability}(\%) = \frac{\text{Absorbance of treated sample}}{\text{Absorbance of control}} \times 100$$

Cytotoxicity enhancement (%) was determined as follows-

$$\text{Cytotoxicity Enhancement}(\%) = (100 - \text{CellViability}_{\text{DOX Loaded NPs}}) - [(100 - \text{Cell Viability}_{\text{NPs}}) + (100 - \text{Cell Viability}_{\text{DOX}})]$$

For each sample, the data (in triplicate) was interpreted as mean \pm standard deviation.

Biocompatibility evaluation of α -KAM-Fe/Mg-CA and DOX- α -KAM-Fe/Mg-CA NPs through hemolysis assay

Freshly drawn blood samples from female Balb/c mice were collected in heparin-coated Eppendorf tubes to prevent blood coagulation. Centrifugation of blood samples was performed at 2000 rpm (10 min, 4 °C), separating the red blood cells (RBCs) (red lower layer) and the plasma (upper yellowish layer). The plasma was removed gently using a micropipette. The RBCs were washed with PBS (3 times), followed by dilution in PBS (20% v/v ratio). For the positive control, deionized water, and negative control, PBS was used. Subsequently, 200 μ L of the prepared samples of α -KAM-CA and α -KAM-Fe/Mg-CA were added to 800 μ L of the diluted stock of RBCs (1/5 dilution of the original sample), and then incubated at 37 °C for an hour. After centrifugation at 4000 rpm (4 °C) for 10 min, the intact erythrocytes were removed from the samples. The supernatants were plated into wells of a 24-well plate, and their absorbance values were recorded with a microplate reader (BIO-RAD-Microplate Reader, Hercules, CA, USA). Data were collected in triplicate as mean value \pm standard deviation (Huang et al. 2016; Neun et al. 2018). The hemolysis ratio was evaluated using the following equation:

$$\text{Hemolysis Ratio}(\%) = \frac{\text{Absorbance}_{\text{Sample}} - \text{Absorbance}_{\text{Negative Control}}}{\text{Absorbance}_{\text{Positive Control}} - \text{Absorbance}_{\text{Negative Control}}} \times 100\%$$

Similarly, the time-dependent hemocompatibility of DOX-loaded α -KAM-CA and DOX-loaded α -KAM-Fe/Mg-CA were evaluated at 30 min, 1 h and 2 h. The samples were prepared in 1 mL bicarbonated DMEM (pH 7.5) via incubation at 37 °C (30 min), with 10% FBS added afterward. The hemolysis assay was performed by the exact same method as mentioned above.

Profiling the protein corona of α -KAM-Fe/Mg-CA NPs through in-solution digestion

α -KAM-Fe/Mg-CA NPs were fabricated with 4 mM Ca^{2+} , 5 μM Fe^{3+} , 12 mM Mg^{2+} , and 4 mM α -KA and α -KAM-CA NPs were generated with 4 mM Ca^{2+} and 4 mM α -KA, in 1 mL bicarbonated DMEM (pH 7.5), through incubation for 30 min at 37 °C and supplementation with 10% FBS and mice plasma, separately. After incubating at 37 °C for 20 min, the particles were centrifuged repeatedly at 13,000 rpm for 15 min. Subsequently, the pellets were solubilized in 100 μ L of 50 mM EDTA and supplemented with 100 mM $(\text{NH}_4)_2\text{CO}_3$ (25 μ L) and (TFE) tetrafluoroethylene (25 μ L). The mixture was reduced in 200 mM (DTT) dithiothreitol solution (1 μ L) and alkylated in 200 mM (IAM) iodoacetamide (4 μ L). Afterward, 100 mM $(\text{NH}_4)_2\text{CO}_3$ solution (100 μ L) was added, and the mixtures were digested with 25 μ L of MS Grade Trypsin (1 $\mu\text{g mL}^{-1}$) for 18 h at 37 °C. In order to halt the reaction, 1 μ L of formic acid was added, followed by overnight speed vacuuming (Mozar et al. 2018).

After that, the samples were mixed with 0.1% formic acid (10 μ L), sonicated, and centrifuged (14,000 \times g, 5 min). Following this, supernatant (5 μ L) in MS tube was transferred to LC-QTOF auto-sampler. The digested peptides were separated in Poroshell 300 Å pore-C18 columns (Agilent, Santa Clara, USA) and eluted with Solution B (90% acetonitrile with 0.1% formic acid), using 5% solution B for 0–30 min and 75% solution B for 30–39 min. A positive quadrupole-time of flight (Q-TOF) polarity was maintained (325 °C, fragmented voltage: 1750 V and 360 V, gas flow: 5 L min^{-1}). The MS scan (acquisition rates: 2 (spectra/s)) was performed at 110–3000 m z^{-1} , while the MS/MS scan (acquisition rates: 4 (spectra/s)) was conducted at 50–3000 m z^{-1} . The spectrums were evaluated with MassHunter software (Agilent

Technologies, Santa Clara, CA, USA) for data acquisition and PEAKS Studio (version 8.0) (Bioinformatics Solutions Inc., Waterloo, ON, Canada). The proteins in mice plasma were detected by integrating database search (SwissProt. *Mus_musculus*) with de novo sequencing, and the proteins in FBS were detected with UniProt protein sequencing software. A homology search was also carried out using PEAKS Studio (version 8.0). For carbamidomethylation, up to 3 mixed cleavages were used with a parent and fragment ion mass tolerance value of 0.1 Da. The filtration effectiveness of the decoy proteins was evaluated using

a false discovery rate (FDR) of 1%, a $-10\lg P$ score > 20 , and ≥ 1 unique peptide. The relative differential changes of proteins were integrated through PEAKS Q protein quantification software. Feature detection of individual samples was carried out through EM (expectation–maximization) algorithm and aligned with the retention time alignment algorithm. A $-10\lg P > 20$ (p value 0.01) displayed the signified peptides. The threshold ratio was presented by a twofold change (represented by value 1) (Mozar et al. 2018; Hossain et al. 2020).

In vivo distribution of α -KAM-Fe/Mg-CA NPs

An investigation into biodistribution was conducted on female Balb/c mice (body weight of 20 to 25 g, 6 to 8 weeks old) acquired from the Animal Facility at the School of Medicine and Health Science, Monash University. The mice were fed ad libitum and provided water in a 12:12 light:dark cycle. Guidelines provided by the facility and Monash Animal Ethics Committee (MARP/2016/126) were followed during the study. 4T1 cells (1×10^5 /mouse) in 180 μL PBS were subcutaneously inoculated into the mammary fat pads of the mice and the tumor was allowed to develop to approximately 75 mm^3 . The tumor-induced mice were intravenously given DOX solution, DOX-loaded α -KAM-CA NPs, and DOX-loaded α -KAM-Fe/Mg-CA NPs (DOX dose: 5 mg kg^{-1}) through the tail vein. After 24 h, the mice were euthanized through cervical dislocation. Next, different organs (brain, spleen, liver, kidney, muscle, heart, and lungs) as well as the tumor were collected and weighed, rinsed with PBS, supplemented with 500 μL sodium fluoride containing Lysis buffer, and kept at -150°C for further study. The organs were further lysed and centrifuged at 8000 rpm (20 min, 4°C). The organs' fluorescence intensity was determined at an excitation (485 nm)/emission (535 nm) spectrum utilizing a 2030 multilabel reader victor X5 (PerkinElmer, Waltham, MA, USA) attached to the PerkinElmer 2030 manager software. The data for each organ were blank corrected utilizing the untreated group and calculated in terms of fluorescence intensity per 500 mg of tissue mass based on mean \pm SEM (Mozar et al. 2018; Karim et al. 2019).

Blood serum analysis

After 24 h of treatment with DOX, DOX-loaded α -KAM-CA, and DOX-loaded α -KAM-Fe/Mg-CA NPs, blood was collected from each mouse ($n=3$ mice per group) to investigate the amount of DOX present in the blood circulatory system. 1 mL syringe with a 25 G (gauge) needle was used to collect the blood from the mice. The mice were euthanized through an auxiliary

approach. The serum was parted from the blood by clotting at room temperature. The samples were then centrifuged at 10,000 rpm (4°C , 20 min). Finally, the serum (200 μL supernatant) was placed on a 96 well OptiPlate (Nunc), and the fluorescence intensity of the samples was measured at excitation (485 nm)/emission (535 nm) wavelengths through a 2030 multilabel reader victor X5 (PerkinElmer, Waltham, MA, USA) connected to the PerkinElmer 2030 manager software. Statistical analysis of the data was performed based on mean and standard deviation (Hossain et al. 2020).

Statistical analysis

The values for each set of data were expressed as mean \pm standard deviation. Statistical analysis was conducted utilizing GraphPad Prism 9 software (San Diego, CA, USA) to evaluate the p values and assess their confidence interval for in vitro and in vivo analysis. T-tests were conducted independently to compare the significant difference between the respective α -KAM-CA and α -KAM-Fe/Mg-CA NPs as well as the NPs-drug complex and the control (free drug). The significance for the measurements of size, surface charge, stability, pH-sensitivity, and drug binding were all tested using T-tests. For in vitro turbidity analysis, cellular uptake, cell viability, and hemolysis, as well as in vivo biodistribution and blood plasma analysis, one-way ANOVA tests were performed using GraphPad software to compare the significance among and between the respective NPs as well as the treated groups (drug-loaded NPs) against the control group. Statistically, the significance level (p value) was deemed to be less than 0.05.

Results and discussion

Effect of α -KA on the growth of Fe/Mg-CA NPs based on measurements of absorbance and optical imaging

The effect of α -KA (Fig. 1) on the growth of the particles was evaluated through turbidity measurement at 320 nm and optical microscopic images. The turbidity of Fe/Mg-CA and CA NPs augmented with a rise in concentrations of α -KA disodium salt hydrate (2 mM, 4 mM, 6 mM, 8 mM, and 10 mM) (Fig. S1). The turbidity of α -KAM-Fe/Mg-CA NPs was, however, a little lower than that of α -KAM-CA NPs (Fig. S1). Perhaps this could be explained by the synergistic effect of exogenous α -KA and Mg^{2+} (as reactants) in significantly reducing aggregation of the resultant particles and thus generating an increasing number of smaller NPs. Furthermore, α -KA likely contributed to the development of a hydrophilic coating on the surface of the NPs (Hossain

et al. 2020), and Mg^{2+} inhibited the growth of the particles by deforming the lattice structural integrity of the apatite NPs through the partial substitution of Ca^{2+} ions (Chowdhury et al. 2004).

The aggregation patterns in Fe/Mg-CA and CA NPs with increasing concentrations of α -KA (i.e., 2 mM, 4 mM, 6 mM, 8 mM, and 10 mM) were verified through optical microscopic images (Fig. S2). The optical micrographs revealed that less aggregation occurred for α -KAM-Fe/Mg-CA NPs compared to α -KAM-CA NPs (Fig. S2). Interestingly, more significant aggregation was observed at 2 mM and 10 mM concentrations of α -KA in both α -KAM-Fe/Mg-CA and α -KAM-CA NPs (Fig. S2). On the contrary, the least aggregation was noticed at 4 mM concentration of α -KA in both cases. This might be because at low concentrations (2 mM), α -KA could not interact efficiently with Fe^{3+} , Mg^{2+} , and Ca^{2+} ions of Fe/Mg-CA NPs and Ca^{2+} ions of CA NPs to render their surfaces sufficiently hydrophilic and retard the aggregation process; while at high concentrations (10 mM), excess free α -KA with its negatively charged domains could act as a bridge linking the cations (i.e., Ca^{2+} , Mg^{2+} , and Fe^{3+}) present in the respective Fe/Mg-CA and CA NPs and form large aggregates. However, 4 mM concentration of α -KA might optimally form hydrophilic surfaces for

α -KAM-Fe/Mg-CA and α -KAM-CA NPs, thereby minimizing the growth or aggregation of the particles.

Measurement of particle diameter and surface potential of α -KAM-Fe/Mg-CA NPs

Stability, plasma half-life, biodistribution, systemic clearance, cellular uptake, drug release, therapeutic efficacy, and toxicity of the NP-drug complex significantly depend on the NPs' size and surface potential (Desai et al. 1997; Kulkarni et al. 2013; Murugan et al. 2015). Smaller particles (10–20 nm) can be rapidly cleared out from the body through glomerular filtration. In contrast, larger particles (greater than 1 μm) can be ingested by mononuclear phagocytic system (MPS) macrophages and may accumulate in the bone marrow, liver, and spleen. Therefore, particles of a 20 nm–1 μm size range with a hydrophilic surface have been proposed to be ideal due to their prolonged blood circulation period, selective extravasation, and lower chance of being eliminated from the body (Chowdhury, 2016; Mozar et al. 2017).

The dynamic light scattering (DLS) method was implemented to determine the hydrodynamic diameter of α -KAM-Fe/Mg-CA and α -KAM-CA NPs through Malvern

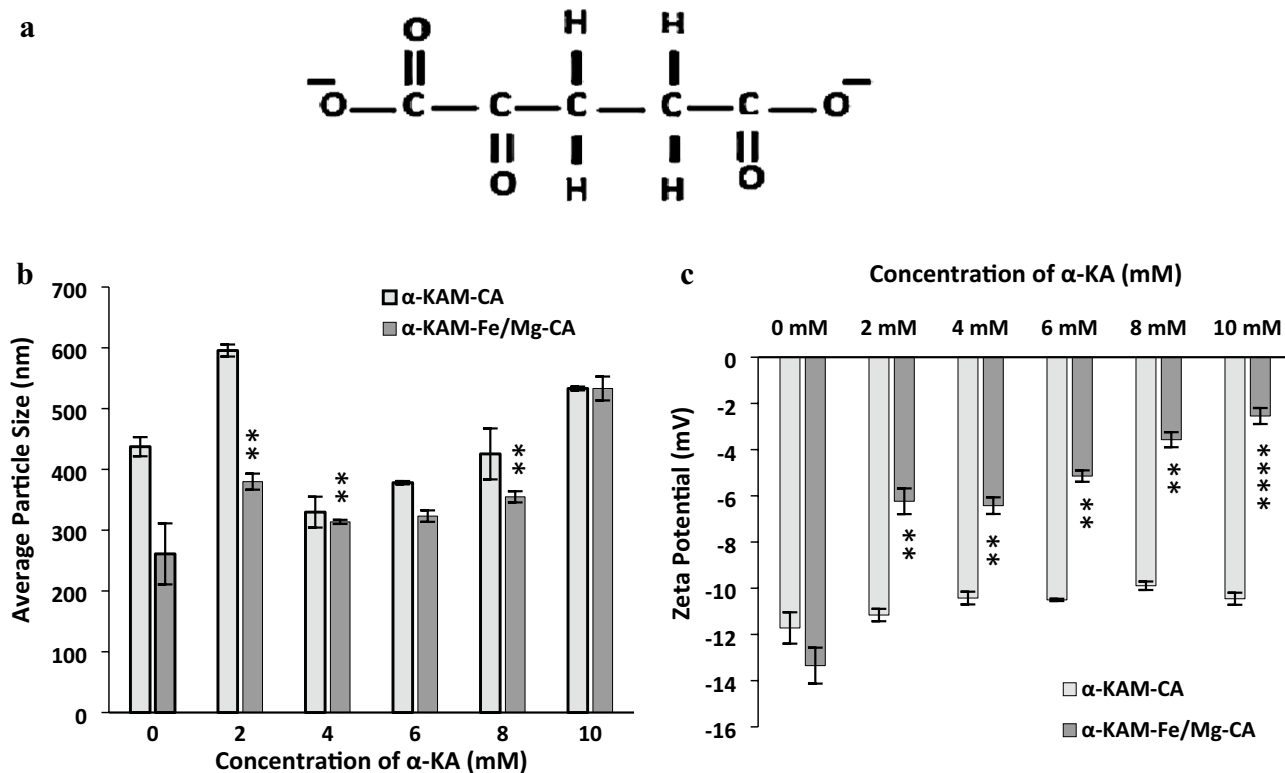


Fig. 1 a Molecular structure of alpha-ketoglutaric acid (α -KA). b The z-average diameters of Fe/Mg-CA and CA NPs fabricated with increasing concentrations (0 mM, 2 mM, 4 mM, 6 mM, 8 mM, and 10 mM) of α -KA. c Zeta potential measurement of Fe/Mg-CA and

CA NPs fabricated with increasing concentrations of α -KA. With a 95% confidence interval, p values between 0.001 and 0.01 (***) were very significant, and less than 0.0001 (****) were extremely significant when comparing α -KAM-CA with α -KAM-Fe/Mg-CA via T-test

nano zeta sizer. As shown in Fig. 1, the average particle size of α -KAM-Fe/Mg-CA NPs was slightly lower than that of α -KAM-CA NPs. This might be owing to the synergistic effect of α -KA and Mg^{2+} in suppressing the particle growth in α -KAM-Fe/Mg-CA. Interestingly, a sharp rise in the particle diameter of α -KAM-Fe/Mg-CA and α -KAM-CA NPs was observed at 2 mM (380 ± 15 nm and 560 ± 15 nm), and 10 mM (533 ± 20 nm and 529 ± 10 nm) concentrations of α -KA. This can be explained by the notion that at 10 mM α -KA concentration, the negative ends of the excess free α -KA might interact with the cations (i.e., Ca^{2+} , Mg^{2+} , and Fe^{3+}) present in the respective Fe/Mg-CA and cause them to aggregate. In contrast, 2 mM concentration of α -KA might be insufficient to reduce the particle size, indicating that α -KA could not interact efficiently with Fe^{3+} , Mg^{2+} and Ca^{2+} ions of Fe/Mg-CA NPs to render their surfaces sufficiently hydrophilic and retard the aggregation process. However, compared to CA and Fe/Mg-CA, the size of the α -KA-modified NPs was slightly larger. This was because the hydrodynamic diameter for α -KA-modified NPs obtained through DLS represented the total size of a particle along with the surface-coated α -KA. Briefly, the size of the Fe/Mg-CA NPs was independent of α -KA concentrations. The microscopic aggregation patterns of the particles generated at 2 mM and 10 mM of α -KA corroborated these observations (Fig. S2).

The average particle size was also measured for the diluted (5, 10, 20, and 50-fold) samples of α -KAM-CA and α -KAM-Fe/Mg-CA NPs in the presence and absence of 10% FBS. Both α -KAM-CA and α -KAM-Fe/Mg-CA demonstrated a decreasing trend in average particle size with the increase in dilution, suggesting that the size of the aggregated particles in high density could be reduced by dispersing in a larger space (Fig. S3). Surprisingly, α -KAM-Fe/Mg-CA NPs in the presence of 10% FBS at 50-fold dilution demonstrated a hydrodynamic diameter of less than 20 nm (Fig. S3). However, in the absence of FBS, the average particle diameter of α -KAM-Fe/Mg-CA NPs was around 750 nm (Fig. S3). These findings, thus, suggest the synergistic effects of FBS and dilution in reducing the particle size.

The surface potential and electrostatic stabilization of the NPs were assessed through zeta potential (ζ) measurement. It was noted that the zeta potential of α -KAM-Fe/Mg-CA NPs was less electronegative than α -KAM-CA NPs (Fig. 1). The less electronegative zeta potential of Fe/Mg-CA NPs compared to CA NPs with increasing concentrations of α -KA might be the result of two negatively charged (carboxyl groups) ends in the backbone of α -KA, displacing more anions (PO_4^{3-} and CO_3^{2-}) in Fe/Mg-CA NPs than CA NPs and interacting with more positively charged domains (Ca^{2+} , Mg^{2+} , Fe^{3+}) of Fe/Mg-CA NPs, making the overall charge more electropositive (Fig. 1). In brief, the zeta potential became less electronegative as the concentration

of α -KA increased. This could be because the negatively charged ends in the backbone of α -KA electrostatically engaged with more cations due to an increase in binding sites at the anionic ends at high concentrations of α -KA.

Evaluation of size distribution through DLS

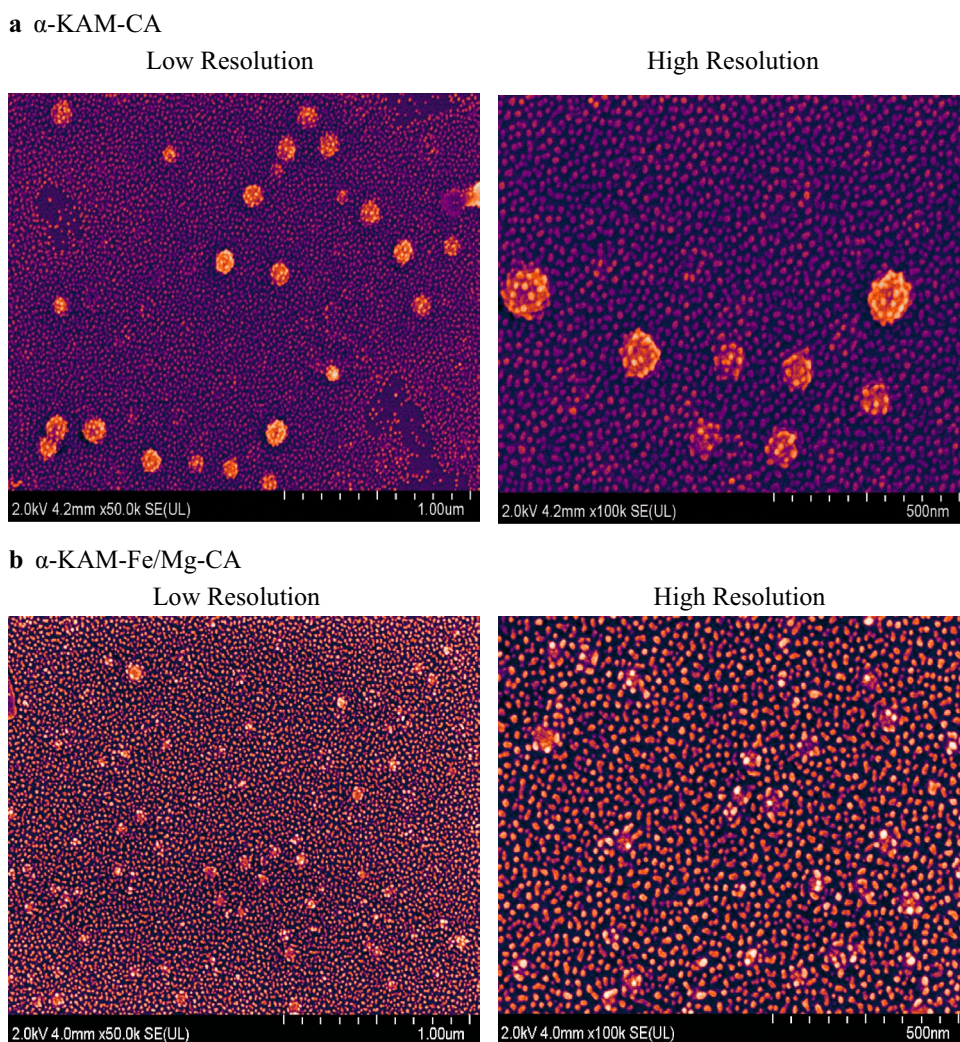
The size distribution of NPs provides information regarding the uniformity and aggregation of the particles as large poly-dispersed particles tend to aggregate and affect the accuracy while measuring the size of the particles (Kaasalainen et al. 2017; Caputo et al. 2019). Size distributions by intensity for the α -KAM-CA and α -KAM-Fe/Mg-CA NPs are presented in Table S1 and Table S2, respectively. For α -KAM-CA and α -KAM-Fe/Mg-CA, the maximum percentage (%) of particles diameter according to size distribution by intensity ranges from 75 to 990 nm (Table S1) and 155 nm to 245 nm (Table S2), respectively. Increasing concentrations (0 mM, 2 mM, 4 mM, 6 mM, 8 mM, and 10 mM) of α -KA were noted, indicating that the size distribution for α -KAM-Fe/Mg-CA NPs was less heterogeneous than α -KAM-CA NPs.

Based on results of absorbance, average particle size, and optical microscopic images, α -KAM-CA formulated with 4 mM Ca^{2+} and 4 mM α -KA, and α -KAM-Fe/Mg-CA generated with 4 mM Ca^{2+} , 5 μ M Fe^{3+} , 12 mM Mg^{2+} , and 4 mM α -KA were chosen for further investigation.

Morphological characterization of α -KAM-Fe/Mg-CA NPs through FESEM

The shape, size, and surface characteristics of α -KAM-CA and α -KAM-Fe/Mg-CA NPs were investigated through FESEM images, revealing that both of the particle types exhibited a spherical shape and displayed good monodispersity. In addition, the high resolution images clearly showed the rough surface morphology for both α -KAM-CA and α -KAM-Fe/Mg-CA NPs (Fig. 2). Notably, the majority of both α -KAM-Fe/Mg-CA and α -KAM-CA particles were relatively smaller in size (15–25 nm) (Fig. 2), which was mainly attributable to the α -KA coating on the NPs' surface. Interestingly, few clusters were observed for both α -KAM-CA (80–150 nm) and α -KAM-Fe/Mg-CA (40–80 nm) NPs (Fig. 2) due to the self-aggregation process. However, the clusters formed with α -KAM-Fe/Mg-CA were smaller, rougher, and both spherical and irregular in shape than those generated with α -KAM-CA (Fig. S4). This could be attributed to the combined effect of Mg^{2+} and α -KA in α -KAM-Fe/Mg-CA NPs, where Mg^{2+} restricted particle growth by partially substituting the Ca^{2+} ions and altering the lattice structure of the apatite NPs (Chowdhury 2013; Haque et al. 2020a, b), and α -KA formed a hydrophilic coating on the surfaces of the respective NPs, preventing them from self-aggregating. These results implied

Fig. 2 Low (scale bar: 1 μm) and high resolution (scale bar: 500 nm) FESEM micrographs. **a** α -KAM-CA. **b** α -KAM-Fe/Mg-CA



that α -KAM-Fe/Mg-CA and α -KAM-CA NPs might enter via clathrin-coated pits rather than through caveolae as the particles were less than 200 nm in diameter (Al-Busaidi et al. 2019). Moreover, they might escape the non-selective clearance by the reticuloendothelial system (RES), which could eventually enhance their tumor accumulation via the EPR effect.

The clusters formed in the NPs were further quantified (Fig. S4). A perfect circle has a circularity value of 1.0 (Takashimizu et al. 2016). When this number is less than 1, it is assumed that clusters are less circular. Additionally, a perfect circle is represented with an aspect ratio of 1. An increasing aspect ratio ($\hat{>}$ 1), on the other hand, indicates an increase in deformation. Interestingly, when the aspect ratio increases, the circularity reduces as well (Takashimizu et al. 2016). From Fig. S4, it was evident that the clusters generated in both α -KAM-CA and α -KAM-Fe/Mg-CA NPs were less circular as their circularity values were less

than 1 and aspect ratios were greater than 1. Furthermore, a roundness value of 1 denoted a completely round structure (Takashimizu et al. 2016). The clusters for α -KAM-CA showed a high degree of roundness ($\hat{>}$ 0.8) (Fig. S4). However, the clusters for α -KAM-Fe/Mg-CA exhibited more fluctuating roundness values ($\hat{>}$ 0.3). These findings suggest that the clusters formed in α -KAM-CA were mostly spherical, while with α -KAM-Fe/Mg-CA, clusters were both spherical and irregular in shapes. Moreover, the surface roughness for the clusters in α -KAM-Fe/Mg-CA was greater compared to α -KAM-CA (Fig. S4). This might be due to the presence of Fe^{3+} in α -KAM-Fe/Mg-CA, which contributed to the rougher morphology of the clusters. Interestingly, the particle diameter captured by FESEM micrographs, however, differed slightly from the average diameter determined by the zeta sizer.

Table 1 Characteristic IR bands for α -KA, α -KAM-CA, and α -KAM-Fe/Mg-CA NPs

Sample	Wave number (cm ⁻¹)	Ionic groups
α -KA	3544, 3427, 3184	Carboxylic acid O–H stretch
	2397, 2281, 1097, 1051	Carboxylic acid C–O stretch
	1709	Ketone
	1575, 1400, 1342	C–H stretch vibration from R–CH ₂ –COOH
α -KAM-CA	3326, 3223	Carboxylic acid O–H stretch
	1641	Ketone
	1480, 1413, 867	CO ₃ ²⁻
	1021, 565	PO ₄ ³⁻
α -KAM-Fe/Mg-CA	3255, 3220	Carboxylic acid O–H stretch
	1640	Ketone
	1413, 866	CO ₃ ²⁻
	1014, 557	PO ₄ ³⁻

Characterization of α -KAM-Fe/Mg-CA NPs through FTIR

The complexation of α -KA with Fe/Mg-CA and CA NPs was verified through FTIR analysis. The FTIR spectrum of α -KA displayed characteristic IR bands which correspond to the ketone group (1709 cm⁻¹), O–H (3544, 3427, 3184 cm⁻¹) group, C–O (2397, 2281, 1097, 1051 cm⁻¹) stretch of carboxylic acid, and C–H (1575, 1400, 1342 cm⁻¹) stretch of R–CH₂–COOH (Fig. S5; Table 1). Furthermore, the peaks at 1410, 1670 cm⁻¹, and 880 cm⁻¹ referred to the CO₃²⁻ group, whereas those at 1000–1100 cm⁻¹ and 550–650 cm⁻¹ were assigned to the PO₄³⁻ group present in both α -KAM-Fe/Mg-CA and α -KAM-CA NPs (Fig. S5) (Chowdhury et al. 2006). However, the CO₃²⁻ peaks in both α -KAM-CA and α -KAM-Fe/Mg-CA might overlap with those of C–H stretch of R–CH₂–COOH. The slight shifting in O–H stretch, ketone group, CO₃²⁻ and PO₄³⁻ in α -KAM-Fe/Mg-CA NPs than α -KAM-CA NPs was probably due to the interactions of Ca²⁺, Fe³⁺, and Mg²⁺ with the negatively charged ends of α -KA, as well as CO₃²⁻ and PO₄³⁻. The shifting of these bands suggested the successful complexation of α -KA with Fe/Mg-CA and CA NPs. The characteristic IR peaks for α -KA, α -KAM-CA, and α -KAM-Fe/Mg-CA NPs are displayed in Table 1 and Fig. S5.

Stability and acid dissolution behavior of α -KAM-Fe/Mg-CA NPs, and pH-responsive DOX release from DOX-loaded α -KAM-Fe/Mg-CA NPs

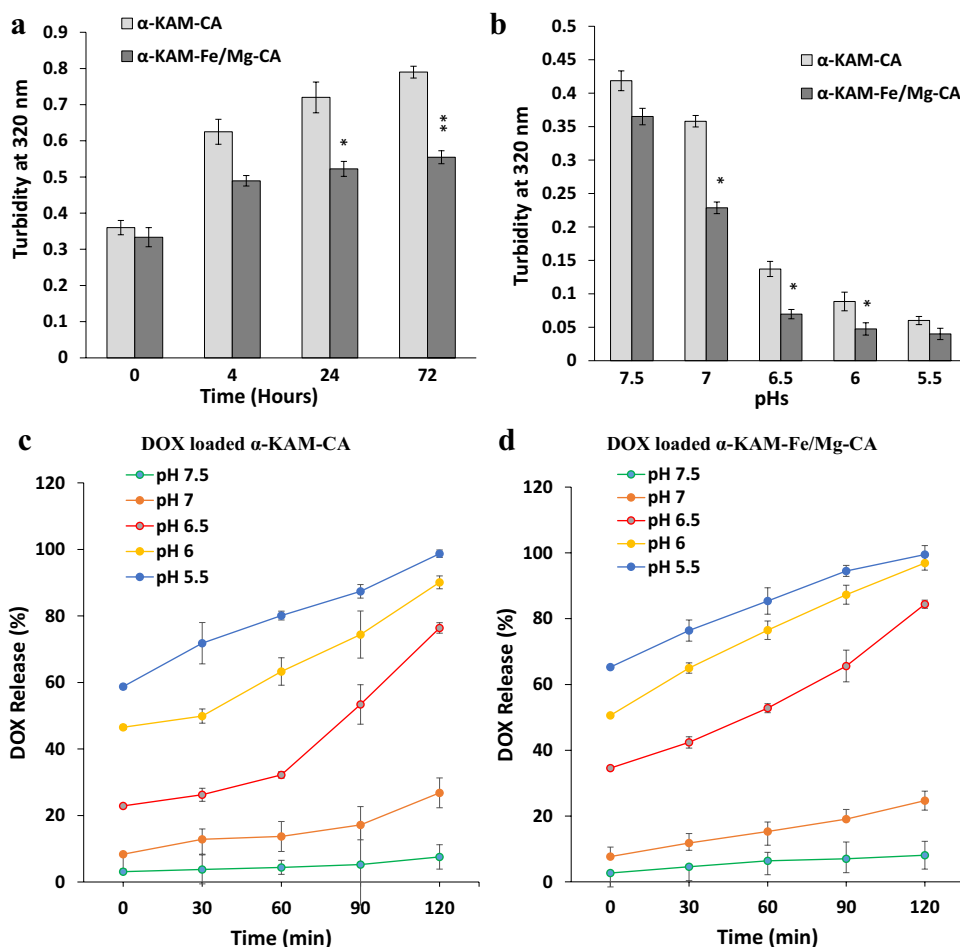
The chemical and physical stability of NPs is crucial in determining the interaction between the NPs and the physiological system. Unstable and agglomerated drug-loaded NPs can result in undesired tissue distribution, triggering chronic immune responses (Ojea-Jimenez et al. 2013). Therefore, stability analysis of α -KAM-Fe/Mg-CA and α -KAM-CA NPs was performed in a time-dependent manner (throughout 72 h) by reading the absorbance of the respective NPs at 320 nm to understand their nature of aggregation in the physiological environment (37 °C, pH 7.5). Both types of NPs demonstrated an ascending trend in turbidity over the incubation period of 72 h (Fig. 3). Interestingly, the turbidity of α -KAM-Fe/Mg-CA NPs was comparatively less than that of α -KAM-CA NPs, suggesting the tendency of the former to agglomerate less and generate particles of a smaller size compared to the latter.

Cancer cells have acidic pH in the extracellular tumor environment (pH 6.5–6.8) in comparison to blood and healthy tissues (pH 7.4). Moreover, the pH further decreases inside the acidic compartments (endosome with pH 5.5–6 or lysosome with pH 4.5–5). This unique feature of tumor tissue allows pH-responsive delivery platforms to effectively release the drug payloads for maximizing the therapeutic activity. Furthermore, an ideal drug delivery system (DDS) will remain in the blood for an extended period until it reaches the site of the tumor, boosting uptake by the cells and promoting the rapid intracellular release of the drug payload (Liu et al. 2005; Lee v 2010; Shi et al., 2015a, b). Therefore, it is crucial to investigate the dissolution of the NPs and the release behavior of drugs from NPs with the change in pH.

The acid dissolution study was undertaken to examine the effects of pH change on the integrity of α -KAM-Fe/Mg-CA NPs. The acid solubility of α -KAM-CA and α -KAM-Fe/Mg-CA NPs was studied by measuring the turbidity (320 nm) with decreasing pHs from pH 7.5 to pH 5.5 (Li et al., 2018). For both α -KAM-CA and α -KAM-Fe/Mg-CA NPs, a notable decrease in turbidity was observed with decreasing pH, thus indicating the almost complete dissolution of the NPs in simulated acidic pH of 6 and 5.5 (Fig. 3).

The pH-dependent release of DOX from α -KAM-Fe/Mg-CA and α -KAM-CA NPs was evaluated over time (0, 30, 60, 90, and 120 min) in five different pHs (pH 7.5, 7, 6.5, 6, 5.5). The highest amount of DOX was released at pH 5.5 from α -KAM-Fe/Mg-CA (65.3% at 0 min, 76.4% at 30 min, 85.4% at 60 min, 94.5% at 90 min and 99.5% at 120 min) and α -KAM-CA (58.7% at 0 min, 71.8% at 30 min, 80.1% at 60 min, 87.4% at 90 min and 98.7% at

Fig. 3 **a** Stability analysis of α -KAM-Fe/Mg-CA and α -KAM-CA NPs through reading the turbidity at 320 nm. The turbidity of the particles was measured at 0, 4, 24, and 72 h. **b** Assessment of acid sensitiveness of α -KAM-CA and α -KAM-Fe/Mg-CA NPs in decreasing pHs (7.5, 7, 6.5, 6, and 5.5). With a 95% confidence interval, p-values between 0.01 and 0.05 (*) were considered significant, and between 0.001 and 0.01 (***) were very significant when comparing α -KAM-CA with α -KAM-Fe/Mg-CA through T-test. **c** pH-dependent release of DOX from α -KAM-CA NPs with time (0, 30, 60, 90, and 120 min) in decreasing pHs. **d** pH-dependent release of DOX from α -KAM-Fe/Mg-CA with time in decreasing pHs



120 min) (Fig. 3). Conversely, at pH 7.5, less than 9% of DOX was released from both α -KAM-Fe/Mg-CA and α -KAM-CA NPs even after 120 min (Fig. 3). This further demonstrates the pH-responsive behavior of α -KAM-Fe/Mg-CA and α -KAM-CA NPs, where DOX release increased with reducing pH. The release of DOX as a result of particle dissolution in acidic endosomal pH could also enhance drug release to the cytosol, achieved by disrupting the endosome through the build-up of osmotic pressure due to the accumulated cations and anions (i.e., Ca^{2+} , Mg^{2+} , Fe^{3+} , CO_3^{2-} , PO_4^{3-}).

Binding affinity of DOX to α -KAM-Fe/Mg-CA NPs

The binding affinity of drugs to NPs is considered among the most significant features of a potential DDS. Factors such as high stability, enhanced solubility, reduced toxicity, greater internalization and stimuli-responsive release efficacy primarily depend on the binding affinity of drugs towards NPs (Shi et al. 2015a, b). Therefore, the efficacy of DOX binding with α -KAM-CA and

α -KAM-Fe/Mg-CA NPs was evaluated in response to elevated concentrations of DOX (1 μM , 2.5 μM , 5 μM , 7.5 μM , and 10 μM). The positively charged DOX was assumed to interact electrostatically with the negatively charged COO^- , CO_3^{2-} , and PO_4^{3-} present in α -KAM-CA and α -KAM-Fe/Mg-CA NPs.

A considerable increase in the binding affinity of DOX for α -KAM-CA and α -KAM-Fe/Mg-CA NPs was observed when the DOX concentrations increased (Fig. S6). However, from 5 μM DOX concentration, no dramatic change in binding efficacy was observed with increasing DOX concentrations, indicating the saturation of their binding sites with DOX. Thus, at 5 μM , 7.5 μM , and 10 μM DOX concentrations, the binding affinity of the respective NPs for DOX was around 25% (Fig. S6). The efficiency of DOX binding with α -KAM-Fe/Mg-CA NPs was slightly more significant than with α -KAM-CA NPs. The smaller size and greater surface area of α -KAM-Fe/Mg-CA NPs might explain this phenomenon, causing the accommodation of a greater amount of the drug within the particles.

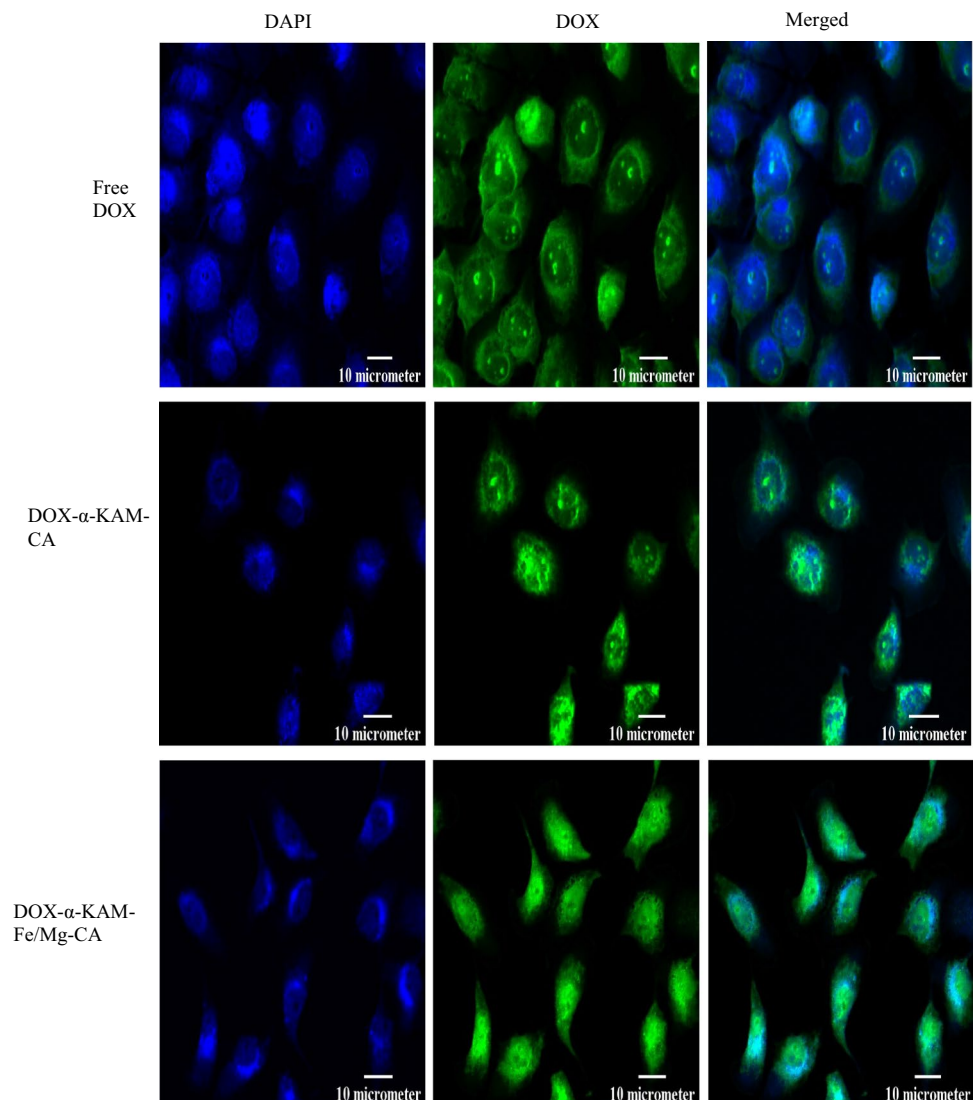
Qualitative and quantitative estimation of cellular uptake for DOX-loaded α -KAM-Fe/Mg-CA NPs under olympus fluorescence microscope and microplate reader

Cellular uptake can enhance the drugs' therapeutic effectiveness by increasing their availability in the cytosol or nucleus and enabling their binding to the targets in order to kill the cancer cells. However, particle size and drug binding affinity of NPs is crucial in enhancing the cellular internalization of NPs-loaded cargos (Shi et al. 2017). Fluorescence micrographs were used to visualize the cellular internalization of DOX carried by α -KAM-CA and α -KAM-Fe/Mg-CA NPs after 4 h of treatment in MCF-7 cells. After 4 h, increased fluorescence intensity was captured for DOX-loaded α -KAM-Fe/Mg-CA NPs and DOX-loaded α -KAM-CA NPs compared to free DOX (Fig. S7). A possible reason involves the small size of α -KAM-Fe/Mg-CA and α -KAM-CA NPs,

facilitating their rapid internalization into the cells. The fluorescence signal was not detected for untreated cells. These images demonstrated that DOX- α -KAM-Fe/Mg-CA NPs could efficiently enter the MCF-7 cells seemingly through endocytosis.

The fluorescence intensity for DOX- α -KAM-Fe/Mg-CA NPs in MCF-7 cells was further quantified through a 2030 multilabel reader victor X5 using the cell lysates. The quantified data were in agreement with the fluorescent micrographs (Fig. S7), indicating significantly higher fluorescence intensity for DOX- α -KAM-Fe/Mg-CA and DOX- α -KAM-CA NPs compared to free DOX after 4 h of treatment for both (Fig. S7). Thus, the maximum cellular uptake that occurred with α -KAM-Fe/Mg-CA and α -KAM-CA NPs could be attributed to their small size.

Fig. 4 Representative confocal laser scanning microscopic images for free DOX, DOX- α -KAM-CA, and DOX- α -KAM-Fe/Mg-CA NPs in MCF-7 cells after 4 h of incubation. The merged region displayed the distribution of DOX (green) in the nucleus (blue, stained with DAPI)



Visualization of intracellular uptake of DOX-loaded α -KAM-Fe/Mg-CA NPs through confocal laser scanning microscope

The uptake and intracellular distribution of DOX- α -KAM-CA and DOX- α -KAM-Fe/Mg-CA in MCF-7 cells was imaged through a confocal laser scanning microscope. The green fluorescence of the captured images revealed a significant rise in the uptake of DOX loaded into α -KAM-CA and α -KAM-Fe/Mg-CA NPs compared to that of free DOX (Fig. 4). Moreover, these images suggest the localization of DOX in the nucleus and throughout the cells. These findings of cellular uptake for DOX- α -KAM-CA and DOX- α -KAM-Fe/Mg-CA NPs were consistent with the fluorescent micrographs captured through Olympus fluorescence microscope IX81 (Shinjuku, Tokyo, Japan) and the quantified results (Fig. S7).

Cytotoxicity and biocompatibility evaluation of α -KAM-Fe/Mg-CA NPs by MTT assay

The antiproliferative effects of α -KAM-CA and α -KAM-Fe/Mg-CA NPs loaded with different concentrations of DOX (i.e., 1 nM, 10 nM, 100 nM, and 1 μ M) were evaluated through MTT colorimetric assay in MCF-7 cells 48 h following treatment. Results confirmed a dose-dependent reduction in the cell viability (%) with increasing DOX concentrations in the case of both α -KAM-CA and α -KAM-Fe/Mg-CA NPs, confirming concentration-dependent toxicity of the DOX-loaded nano-carriers. However, the cytotoxic effect was more noticeable for DOX-loaded α -KAM-CA and α -KAM-Fe/Mg-CA NPs in comparison to free DOX (Fig. S8). These results suggest that the small size of the DOX-loaded α -KA modified NPs aided successful cellular internalization and effective release of DOX inside the cells, resulting in the apoptosis of cancer cells. As compared to DOX-loaded α -KAM-CA, no significant difference in the cell viability (%) was observed for DOX-loaded α -KAM-Fe/Mg-CA NPs (Fig. S8). The cell viability (%) of α -KAM-CA and α -KAM-Fe/Mg-CA NPs was approximately 87%, indicating the biocompatibility of the nano-carriers. The 13% cell growth inhibitory effect of the NPs was due to the deposition of NPs on the surface of the cells as a result of the small space in the 24-well plate. The overall cytotoxicity enhancement (%) of DOX- α -KAM-Fe/Mg-CA NPs was slightly higher than that of DOX- α -KAM-CA NPs (Fig. S8). The dosage independent cytotoxicity enhancement of DOX in α -KAM-CA and α -KAM-Fe/Mg-CA NPs might be attributable to a variety of factors, including cellular uptake, NP size and surface properties, cell internalization mechanism, cell type, and the duration of treatment with DOX loaded NPs in cells (Xue et al. 2010; Warheit et al. 2007; Fatemian et al. 2018; Roszak et al. 2020; Xu et al. 2021). Thus, the cell

viability study highlights that α -KAM-CA and α -KAM-Fe/Mg-CA NPs could elevate the toxic effects of drugs in MCF-7 cells owing to the increased cellular internalization.

Biocompatibility evaluation of α -KAM-Fe/Mg-CA and DOX- α -KAM-Fe/Mg-CA NPs through hemolysis assay

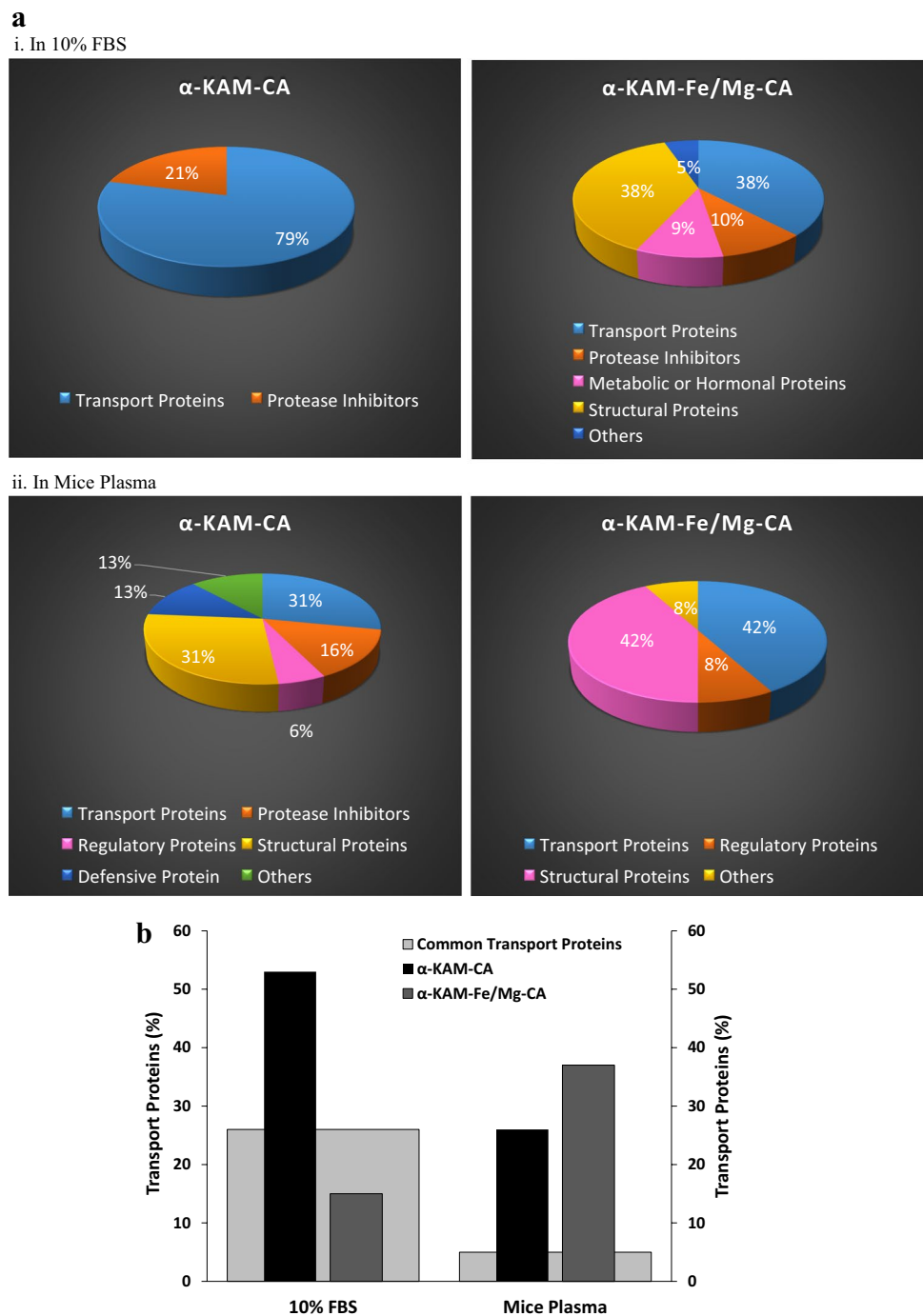
In the hemolysis assay, the hemoglobin released as a result of the RBC rupture (due to imbalance in osmotic pressures or physical changes in the blood) was measured to determine the biocompatibility of the NPs. The hemolytic activities of α -KAM-CA and α -KAM-Fe/Mg-CA NPs were assessed using hemolysis assay with the blood of female Balb/c mice. In this study, deionized water was taken as the positive control and PBS as the negative control. As shown in Table S3 (Fig. S9), the hemolytic ratios for both α -KAM-CA and α -KAM-Fe/Mg-CA NPs were similar, accounting for $0.06\% \pm 0.002$ and $0.07\% \pm 0.018$, respectively, demonstrating a hemolytic ratio of less than 1%. According to the American Society for Clinical Pathology, a hemolysis ratio of less than 2% was considered nonhemolytic (Lowe et al. 2008; Mazzarino et al. 2015). The positive control showed complete hemolysis (Fig. S9). Thus, α -KAM-CA and α -KAM-Fe/Mg-CA NPs were blood compatible.

A time-dependent hemolytic assay was performed to elucidate the biocompatibility of DOX-loaded α -KAM-CA and DOX-loaded α -KAM-Fe/Mg-CA NPs. It was observed that the hemolysis induced by free DOX was more abrupt with time (30 min, 1 h, 2 h) compared to the DOX-loaded α -KAM-CA and DOX-loaded α -KAM-Fe/Mg-CA NPs (Fig. S9). The hemolytic rate was lower than 1% for both DOX- α -KAM-CA and DOX- α -KAM-Fe/Mg-CA NPs (Fig. S9), and no significant change in hemolysis was observed with time. Since the hemolysis depends on the surface charge of the NPs, the lower rate of hemolysis in the case of DOX- α -KAM-CA and DOX- α -KAM-Fe/Mg-CA NPs might be because of the negative charge (COOH^- , PO_4^{3-} , CO_3^{2-}) on the NPs, which obstruct their interaction with the RBCs due to the electrostatic repulsion.

Identification of serum proteins interacting with α -KAM-Fe/Mg-CA NPs through in-solution digestion

When NPs are administered inside the body, they can be recognized as foreign particles by the body's defense system after being coated with selected serum proteins known as opsonins along with other proteins as part of the 'protein corona' spontaneously developed on the particles. Therefore, it is imperative to know the identity of the proteins adsorbed onto the NPs. Furthermore, protein corona-mediated targeting can be harnessed to manipulate the interaction of specific

Fig. 5 **a** Pie charts representing the relative abundance (%) of the identified proteins in (i) 10% FBS and (ii) mice plasma for α -KAM-CA and α -KAM-Fe/Mg-CA NPs based on their biological functions. **b** Overlapping bar chart demonstrating the common transport proteins (expressed in %) identified for both α -KAM-CA and α -KAM-Fe/Mg-CA NPs in 10% FBS and mice plasma



plasma proteins on the surface of the engineered NPs. Such controlled manipulation can direct the engineered NPs towards specific areas of the body, stimulate or suppress the immune cell responses, affect the elimination of NPs from the body through opsonization, extend the circulation time of NPs, enhance their cellular internalization, modulate the cellular pathways, and protect RBCs from NPs-mediated hemolysis (Singh et al. 2009; Lee et al. 2015; Karimi et al. 2016; Zanganeh et al. 2016; Mozar et al. 2018).

Protein corona analysis of α -KAM-CA and α -KAM-Fe/Mg-CA NPs in 10% FBS and mice plasma was performed through the in-solution digestion of trypsin by LCMS to identify the proteins interacting with the respective NPs. The relative abundance of the identified proteins in 10% FBS and mice plasma for α -KAM-CA and α -KAM-Fe/Mg-CA NPs in terms of their physiological functions are expressed in pie charts (Fig. 5). The common transport proteins of total transport proteins detected for both

α -KAM-CA and α -KAM-Fe/Mg-CA in 10% FBS and mice plasma are displayed in the overlapping bar chart (Fig. 5). In 10% FBS, α -KAM-CA NPs interacted only with transport proteins (79%) and protease inhibitors (21%), whereas α -KAM-Fe/Mg-CA NPs revealed a preference for transport proteins (38%), protease inhibitors (10%), metabolic proteins (9%), structural proteins (38%), and other types of proteins (5%) (Fig. 5, Table S4). As can be seen from Fig. 5 as well as Tables S4 and S5, the respective NPs in both 10% FBS and mice plasma showed interactions with transport proteins (dysopsonins such as serum albumin and apolipoproteins), which could extend their circulation time in blood, mitigate systemic toxicity, and increase their distribution at the cancer site via the EPR effect. Also, binding with serum albumin could inhibit the uptake by monocytes and enhance cellular internalization (Corbo et al. 2016). Notably, the NPs demonstrated no interaction with opsonins which could facilitate their clearance from the body, and apolipoprotein A4 and apolipoprotein C3 which could reduce their cellular internalization (Nguyen et al. 2017). However, both α -KAM-CA and α -KAM-Fe/Mg-CA NPs in 10% FBS, and α -KAM-CA in mice plasma showed affinity towards apolipoprotein A1 and protease inhibitors. Interaction of NPs with apolipoprotein A1 could foster their delivery into the central nervous system (CNS) and could enable the NPs to cross the blood–brain barrier (BBB) (Tables S4 and S5) (Zensi et al. 2009). On the other hand, proteases were reported to be involved in a variety of activities related to tumor formation and progression. Therefore, they could serve as a foundation for membrane and matrix disintegration, chemotherapy inactivation, cell viability regulation, immune response modulation, and recruitment of inflammatory cells (Rudzińska et al. 2021). Furthermore, proteases found in internal compartments such as the cytoplasm, mitochondria, and nucleus were linked to a variety of signaling pathways that could increase growth, motility, adhesion and de-differentiation in cancer cells (Zivotovsky et al. 1997; Rudzińska et al. 2019). As a result, the interaction of NPs with protease inhibitors might be beneficial as the proteolytic inhibition of proteases by inhibitors could naturally reduce cancer cell proliferation and migration. In mice plasma, both α -KAM-CA (42%) and α -KAM-Fe/Mg-CA NPs (42%) exhibited maximum selectivity towards structural proteins (Fig. 5, Table S5). Subtypes of keratin (structural proteins) have been found to play an essential role in the transition between epithelial and mesenchymal tissues, particularly in malignant breast cancer cells, where they might convert the intermediate filaments (anchored to epithelial cells) into keratin and vimentin (Hendrix et al. 1997). That said, vimentin overexpression could boost the spread and invasiveness in cancer cells (Hendrix

et al. 1997). Fortunately, α -KAM-Fe/Mg-CA NPs in mice plasma showed significantly less interaction with any keratin filaments in mice plasma (Table S5).

Interestingly, in 10% FBS, the number of plasma proteins interacting with α -KAM-Fe/Mg-CA NPs was more than α -KAM-CA. On the contrary, with mice plasma, the plasma proteins that interact with α -KAM-Fe/Mg-CA NPs were less compared to α -KAM-CA NPs. The

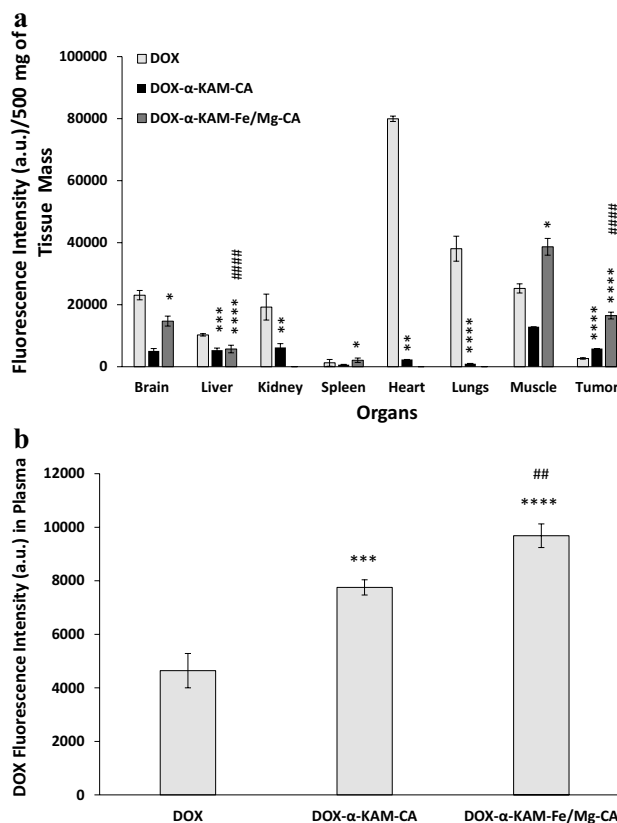


Fig. 6 **a** Distribution of DOX in tumor and other organs after 24 h of treatment with free DOX, DOX loaded α -KAM-CA, and DOX loaded α -KAM-Fe/Mg-CA NPs in Balb/c mice. With a 95% confidence interval, p values between 0.01 and 0.05 (*) were considered significant, between 0.001 and 0.01 (**) were very significant, between 0.0001 and 0.001 (***) were highly significant and less than 0.0001 (****) were extremely significant when comparing control (DOX) and treatment (DOX bound NPs) via one-way ANOVA analysis. Similarly, p-values less than 0.0001 (####) were extremely significant when comparing DOX- α -KAM-CA with DOX- α -KAM-Fe/Mg-CA via one-way ANOVA analysis. **b** DOX fluorescence intensity in the blood plasma of Balb/c 4T1 mammary tumor-bearing mice following 24 h of intravenous administration of DOX solution, DOX-loaded α -KAM-CA, and DOX-loaded α -KAM-Fe/Mg-CA NPs through the tail vein. With a 95% confidence interval, p values between 0.0001 and 0.001 (***) were highly significant and less than 0.0001 (****) were extremely significant when comparing control (DOX) and treatment (DOX bound NPs) via one-way ANOVA tests. Likewise, p values between 0.001 and 0.01 (##) were very significant when comparing DOX- α -KAM-CA with DOX- α -KAM-Fe/Mg-CA via one-way ANOVA analysis

majority of the identified proteins for both α -KAM-CA and α -KAM-Fe/Mg-CA NPs in 10% FBS as well as mice plasma possess an isoelectric point (pI) < 7.5 , indicating their negatively charged surface in biological pH, which might help them electrostatically interact with the positively charged ions in α -KAM-CA (Ca^{2+}) and α -KAM-Fe/Mg-CA (Ca^{2+} , Mg^{2+} , and Fe^{3+}) NPs. The proteins were classified into groups based on their physiological role and presented in Tables S4 and S5, along with their molecular weight (Da) and pI values.

Biodistribution study at 24 H Post intravenous treatment with α -KAM-Fe/Mg-CA NPs

Biodistribution analysis was conducted to investigate the distribution, and potential toxicity of free DOX, DOX-loaded α -KAM-CA, and DOX-loaded α -KAM-Fe/Mg-CA NPs in the tumor and other tissues such as heart, lung, spleen, liver, brain, muscle, and kidney. The experiment was conducted with 6 to 8 week old subcutaneously induced 4T1 mammary tumor-induced Balb/c mice at 24 h post intravenous treatment. The mice were randomly distributed into three groups ($n=3$). The accumulation of α -KAM-Fe/Mg-CA NPs in the tumor was considerably higher than α -KAM-CA NPs and free DOX, indicating their successful delivery at the tumor site through the EPR effect (Fig. 6). Thus, NPs were able to penetrate the tumor site as a result of the leaky vasculature of the tumor blood vessels and accumulate there for an extended period due to impeded lymphatic drainage, which might lead to a site-specific anticancer effect at the malignant site. Interestingly, α -KAM-Fe/Mg-CA NPs showed no DOX distribution in the heart, lungs, and kidneys (Fig. 6). This might be due to the presence of the hydrophilic layer of α -KA as well as the Fe^{3+} and Mg^{2+} , which formed a protein corona (ligands) not identified by the receptors present in the heart, lung, and kidney tissues, therefore inhibiting their accumulation in the heart, lung, and kidney to potentially prevent cardiotoxicity, pulmonary toxicity, and nephrotoxicity, respectively. The distribution of free DOX in the heart was significantly (34.2-fold) greater than α -KAM-CA NPs, suggesting alleviated cardiotoxicity of the anthracycline drug, which might be due to its small size, enabling it to penetrate the tight junctions of the cardiac muscles. A decreased fluorescence signal was noticed for α -KAM-Fe/Mg-CA NPs in the spleen and liver in contrast to free DOX (Fig. 6). The accumulation in the liver and spleen might be related to the macrophage uptake of NPs in the RES. When NPs were retained in RES organs, they failed to target tumors and penetrate effectively into them, resulting in reduced drug delivery at the targeted site of the tumor (Tang et al. 2019). However, free DOX exerted a 1.6-fold greater accumulation in the brain compared to α -KAM-Fe/Mg-CA NPs. The deposition of α -KAM-Fe/Mg-CA NPs in the brain might be

due to their tendency to cross the blood–brain barrier (BBB) as a result of their affinity towards apolipoprotein A1 as confirmed by the protein corona analysis (Tables S4 and S5). It was reported that apolipoprotein A1 could potentially cross the BBB via clathrin-independent and cholesterol-mediated endocytosis (Zhou et al. 2019). Notably, extremely high fluorescence intensity was detected for α -KAM-Fe/Mg-CA NPs in the muscles, denoting the risk of their muscular toxicity. Moreover, during the experimental period, the mice displayed no behavioral changes.

The amounts of DOX present in the blood at 24 h post-treatment with free DOX, DOX-loaded α -KAM-CA, and DOX-loaded α -KAM-Fe/Mg-CA NPs were evaluated and assessed by quantifying the fluorescence intensity of the blood collected from each Balb/c mice ($n=3$ /group). The fluorescence intensity of DOX-loaded α -KAM-Fe/Mg-CA NPs was 1.2-fold greater than that of DOX-loaded α -KAM-CA and 2.1-fold greater than free DOX (Fig. 6), suggesting their extended circulation period in the bloodstream and enhanced accumulation in cancer cells via EPR effect.

In summary, it could be said that the transportation of DOX-loaded α -KAM-Fe/Mg-CA NPs into tumor tissues was primarily influenced by their particle size, which subsequently modulated their plasma half-life, cellular internalization, and release of the drug into the tumor. Plasma half-life was directly related to their circulation velocity and aggregation in blood, hence regulating their endocytosis pathway, in vivo permeation and distribution, as well as impacting the drug's intracellular accumulation and effectiveness (Yue et al. 2010; Kim et al. 2011). Furthermore, the protein corona profile of α -KAM-Fe/Mg-CA NPs in both 10% FBS and mouse plasma revealed their affinity for transport proteins, which played a key role in their prolonged blood circulation period and drug distribution at the cancer site. Thereby, it is apparent that both the size and the protein corona profile of the α -KAM-Fe/Mg-CA NPs had a profound influence on their biodistribution.

Conclusion

Complexation of α -KA with Fe/Mg-CA offers great promise in generating NPs of nano-size dimension with PDI values and self-aggregation tendencies lower than α -KAM-CA NPs. The DOX binding affinity of the former was slightly more significant than the latter. DOX-loaded α -KAM-Fe/Mg-CA NPs revealed prominent cellular internalization, fast release of DOX at highly acidic pH of endosomes while maintaining stability in physiological pH. The cytotoxicity study in MCF-7 cells demonstrated the high toxicity of DOX-loaded α -KAM-Fe/Mg-CA NPs than free DOX. The protein corona analysis showed interactions of α -KAM-Fe/

Mg-CA NPs with dysopsonins (serum albumin and apolipoproteins) as well as transport proteins, which could extend their circulation in the bloodstream. These findings resembled the obtained data from the blood plasma analysis, which also indicated an increased circulation period of DOX for DOX-loaded α -KAM-Fe/Mg-CA NPs. The animal biodistribution study of DOX-loaded α -KAM-Fe/Mg-CA NPs displayed a greater accumulation of DOX at the tumor site compared to free DOX and DOX-loaded α -KAM-CA NPs. Moreover, DOX-loaded α -KAM-Fe/Mg-CA NPs demonstrated no DOX accumulation in the heart, lung, and kidney, revealing their tendency to prevent cardiotoxicity, pulmonary toxicity, and nephrotoxicity. Also, its distribution in the liver and spleen was less compared to free DOX. Thereby, these preliminary findings suggest that the physicochemical features of α -KAM-Fe/Mg-CA NPs might have the potential to improve their pharmacokinetic profile and result in enhanced therapeutic efficacy. Hence, α -KAM-Fe/Mg-CA NPs could be a useful DDS in treating breast cancer.

Supplementary Information The online version contains supplementary material available at <https://doi.org/10.1007/s40005-022-00571-1>.

Acknowledgements The project was financially supported by an FRGS grant from the Ministry of Education, Malaysia (FRGS/1/2018/STG05/MUSM/02/3).

Funding Open Access funding enabled and organized by CAUL and its Member Institutions.

Declarations

Conflict of interest All authors (S.T. Haque, Md. E. Karim, I. Othman, and E.H. Chowdhury) declare that they have no conflict of interest in the content of this work.

Research involving human and animal participants Animal studies were performed after receiving approval from the Monash University Animal Ethics Committee (MARF/2016/126). All applicable international, national, and/or institutional guidelines provided by the Animal Facility and Monash University Animal Ethics Committee were followed during the study.

Open Access This article is licensed under a Creative Commons Attribution 4.0 International License, which permits use, sharing, adaptation, distribution and reproduction in any medium or format, as long as you give appropriate credit to the original author(s) and the source, provide a link to the Creative Commons licence, and indicate if changes were made. The images or other third party material in this article are included in the article's Creative Commons licence, unless indicated otherwise in a credit line to the material. If material is not included in the article's Creative Commons licence and your intended use is not permitted by statutory regulation or exceeds the permitted use, you will need to obtain permission directly from the copyright holder. To view a copy of this licence, visit <http://creativecommons.org/licenses/by/4.0/>.

References

- Abandansari HS, Nabid MR, Rezaei SJT, Niknejad H (2014) pH-sensitive nanogels based on Boltorn® H40 and poly (vinylpyridine) using mini-emulsion polymerization for delivery of hydrophobic anticancer drugs. *Polymer* 55:3579–3590
- Al-Busaidi H, Karim M, SaZ A, Tha KK, Chowdhury EH (2019) Magnesium fluoride forms unique protein corona for efficient delivery of doxorubicin into breast cancer cells. *Toxics* 7:10
- Attia MF, Anton N, Wallyn J, Omran Z, Vandamme TF (2019) An overview of active and passive targeting strategies to improve the nanocarriers efficiency to tumour sites. *J Pharm Pharmacol* 71:1185–1198
- Bae KH, Chung HJ, Park TG (2011) Nanomaterials for cancer therapy and imaging. *Mol Cells* 31:295–302
- Caputo F, Clogston J, Calzolari L, Rösslein M, Prina-Mello A (2019) Measuring particle size distribution of nanoparticle enabled medicinal products, the joint view of EUNCL and NCI-NCL. A step by step approach combining orthogonal measurements with increasing complexity. *J Control Release* 299:31–43
- Carvalho C, Santos RX, Cardoso S, Correia S, Oliveira PJ, Santos MS, Moreira PI (2009) Doxorubicin: the good, the bad and the ugly effect. *Curr Med Chem* 16:3267–3285
- Cho K, Wang X, Nie S, Chen ZG, Shin DM (2008) Therapeutic nanoparticles for drug delivery in cancer. *Clin Cancer Res* 14:1310–1316
- Chowdhury E (2007) pH-sensitive nano-crystals of carbonate apatite for smart and cell-specific transgene delivery. *Expert Opin Drug Deliv* 4:193–196
- Chowdhury EH (2013) pH-responsive magnesium-and carbonate-substituted apatite nano-crystals for efficient and cell-targeted delivery of transgenes.
- Chowdhury EH (2016) *Nanotherapeutics: from laboratory to clinic*. CRC press
- Chowdhury E, Kunou M, Nagaoka M, Kundu A, Hoshiba T, Akaike T (2004) High-efficiency gene delivery for expression in mammalian cells by nanoprecipitates of Ca–Mg phosphate. *Gene* 341:77–82
- Chowdhury E, Maruyama A, Kano A, Nagaoka M, Kotaka M, Hirose S, Kunou M, Akaike T (2006) pH-sensing nano-crystals of carbonate apatite: effects on intracellular delivery and release of DNA for efficient expression into mammalian cells. *Gene* 376:87–94
- Corbo C, Molinaro R, Parodi A, Toledano Furman NE, Salvatore F, Tasciotti E (2016) The impact of nanoparticle protein corona on cytotoxicity, immunotoxicity and target drug delivery. *Nanomedicine* 11:81–100
- Cui T, Zhang S, Sun H (2017) Co-delivery of doxorubicin and pH-sensitive curcumin prodrug by transferrin-targeted nanoparticles for breast cancer treatment. *Oncol Rep* 37:1253–1260
- Desai MP, Labhasetwar V, Walter E, Levy RJ, Amidon GL (1997) The mechanism of uptake of biodegradable microparticles in Caco-2 cells is size dependent. *Pharm Res* 14:1568–1573
- Dong X, Mumper RJ (2010) Nanomedicinal strategies to treat multidrug-resistant tumors: current progress. *Nanomedicine* 5:597–615
- Donnarumma F, Wintersteiger R, Schober M, Greilberger J, Matzi V, Maier A, Schwarz M, Ortner A (2013) Simultaneous quantitation of alpha-ketoglutaric acid and 5-hydroxymethylfurfural in plasma by HPLC with UV and fluorescence detection. *Anal Sci* 29:1177–1182
- Fatemian T, Chowdhury EH (2018) Cytotoxicity enhancement in breast cancer cells with carbonate apatite-facilitated intracellular delivery of anti-cancer drugs. *Toxics* 6:12

- Filip R, Pierzynowski SG (2007) The role of glutamine and alfa-ketoglutarate in gut metabolism and the potential application in medicine and nutrition. *J Pre-Clin Clin Res* 1
- Gao W, Chan JM, Farokhzad OC (2010) pH-responsive nanoparticles for drug delivery. *Mol Pharm* 7:1913–1920
- Haque ST, Chowdhury EH (2018) Recent progress in delivery of therapeutic and imaging agents utilizing organic-inorganic hybrid nanoparticles. *Curr Drug Deliv* 15:485–496
- Haque ST, Islam RA, Gan SH, Chowdhury EH (2020a) Characterization and evaluation of bone-derived nanoparticles as a novel pH-responsive carrier for delivery of doxorubicin into breast cancer cells. *Int J Mol Sci* 21:6721
- Haque ST, Karim M, SaZ A, Othman I, Holl MMB, Chowdhury EH (2020b) Fe/Mg-modified carbonate apatite with uniform particle size and unique transport protein-related protein corona efficiently delivers doxorubicin into breast cancer cells. *Nanomaterials* 10:834
- Hatakeyama H (2017) Recent advances in endogenous and exogenous stimuli-responsive nanocarriers for drug delivery and therapeutics. *Chem Pharm Bull* 65:612–617
- Hendrix M, SefTOR EA, SefTOR R, Trevor KT (1997) Experimental co-expression of vimentin and keratin intermediate filaments in human breast cancer cells results in phenotypic interconversion and increased invasive behavior. *Am J Pathol* 150:483
- Hortobagyi G (1997) Anthracyclines in the treatment of cancer. *Drugs* 54:1–7
- Hossain SM, Chowdhury EH (2018) Citrate-and succinate-modified carbonate apatite nanoparticles with loaded doxorubicin exhibit potent anticancer activity against breast cancer cells. *Pharmaceutics* 10:32
- Hossain SM, Shetty J, Tha KK, Chowdhury EH (2019) α -Ketoglutaric acid-modified carbonate apatite enhances cellular uptake and cytotoxicity of a raf-kinase inhibitor in breast cancer cells through inhibition of MAPK and PI-3 kinase pathways. *Biomedicines* 7:4
- Hossain SM, Abidin Z, Asnawi S, Chowdhury EH (2020) Krebs cycle intermediate-modified carbonate apatite nanoparticles drastically reduce mouse tumor burden and toxicity by restricting broad tissue distribution of anticancer drugs. *Cancers* 12:161
- Huang H, Lai W, Cui M, Liang L, Lin Y, Fang Q, Liu Y, Xie L (2016) An evaluation of blood compatibility of silver nanoparticles. *Sci Rep* 6:25518
- Kaasalainen M, Aseyev V, Von Haartman E, Karaman DŞ, Mäkilä E, Tenhu H, Rosenholm J, Salonen J (2017) Size, stability, and porosity of mesoporous nanoparticles characterized with light scattering. *Nanoscale Res Lett* 12:1–10
- Karim ME, Shetty J, Islam RA, Kaiser A, Bakhtiar A, Chowdhury EH (2019) Strontium sulfite: a new pH-responsive inorganic nanocarrier to deliver therapeutic siRNAs to cancer cells. *Pharmaceutics* 11:89
- Karimi M, Bahrami S, Ravari SB, Zangabad PS, Mirshekari H, Bozorgomid M, Shahreza S, Sori M, Hamblin MR (2016) Albumin nanostructures as advanced drug delivery systems. *Expert Opin Drug Deliv* 13:1609–1623
- Kim S, Oh W-K, Jeong YS, Hong J-Y, Cho B-R, Hahn J-S, Jang J (2011) Cytotoxicity of, and innate immune response to, size-controlled polypyrrole nanoparticles in mammalian cells. *Biomaterials* 32:2342–2350
- Kulkarni SA, Feng S-S (2013) Effects of particle size and surface modification on cellular uptake and biodistribution of polymeric nanoparticles for drug delivery. *Pharm Res* 30:2512–2522
- Kumari A, Yadav SK, Yadav SC (2010) Biodegradable polymeric nanoparticles based drug delivery systems. *Colloids Surf, B* 75:1–18
- Lee CH, Cheng SH, Huang IP, Souris JS, Yang CS, Mou CY, Lo LW (2010) Intracellular pH-responsive mesoporous silica nanoparticles for the controlled release of anticancer chemotherapeutics. *Angew Chem Int Ed* 49:8214–8219
- Lee YK, Choi E-J, Webster TJ, Kim S-H, Khang D (2015) Effect of the protein corona on nanoparticles for modulating cytotoxicity and immunotoxicity. *Int J Nanomed* 10:97
- Li S-D, Huang L (2009) Nanoparticles evading the reticuloendothelial system: role of the supported bilayer. *Biochimica Et Biophysica Acta (BBA)-Biomembranes* 1788:2259–2266
- Li H-J, Du J-Z, Liu J, Du X-J, Shen S, Zhu Y-H, Wang X, Ye X, Nie S, Wang J (2016) Smart superstructures with ultrahigh pH-sensitivity for targeting acidic tumor microenvironment: instantaneous size switching and improved tumor penetration. *ACS Nano* 10:6753–6761
- Li L, Wang J, Kong H, Zeng Y, Liu G (2018) Functional biomimetic nanoparticles for drug delivery and theranostic applications in cancer treatment. *Sci Technol Adv Mater* 19:771–790
- Liu S, Tong Y, Yang Y-Y (2005) Incorporation and in vitro release of doxorubicin in thermally sensitive micelles made from poly (N-isopropylacrylamide-co-N, N-dimethylacrylamide)-b-poly (D, L-lactide-co-glycolide) with varying compositions. *Biomaterials* 26:5064–5074
- Lowe G, Stike R, Pollack M, Bosley J, O'brien P, Hake A, Landis G, Billings N, Gordon P, Manzella S (2008) Nursing blood specimen collection techniques and hemolysis rates in an emergency department: analysis of venipuncture versus intravenous catheter collection techniques. *J Emerg Nurs* 34:26–32
- Lu Y-J, Lin P-Y, Huang P-H, Kuo C-Y, Shalumon K, Chen M-Y, Chen J-P (2018) Magnetic graphene oxide for dual targeted delivery of doxorubicin and photothermal therapy. *Nanomaterials* 8:193
- Mazzarino L, Loch-Neckel G, Dos Santos BL, Ourique F, Otsuka I, Halila S, Curi Pedrosa R, Santos-Silva MC, Lemos-Senna E, Curti Muniz E (2015) Nanoparticles made from xyloglucan-block-poly-caprolactone copolymers: safety assessment for drug delivery. *Toxicol Sci* 147:104–115
- Mozar FS, Chowdhury EH (2017) Surface-modification of carbonate apatite nanoparticles enhances delivery and cytotoxicity of gemcitabine and anastrozole in breast cancer cells. *Pharmaceutics* 9:21
- Mozar FS, Chowdhury EH (2018) PEGylation of carbonate apatite nanoparticles prevents opsonin binding and enhances tumor accumulation of gemcitabine. *J Pharm Sci* 107:2497–2508
- Murugan K, Choonara YE, Kumar P, Bujukumar D, Du Toit LC, Pillay V (2015) Parameters and characteristics governing cellular internalization and trans-barrier trafficking of nanostructures. *Int J Nanomed* 10:2191
- Nakamura Y, Mochida A, Choyke PL, Kobayashi H (2016) Nanodrug delivery: is the enhanced permeability and retention effect sufficient for curing cancer? *Bioconjug Chem* 27:2225–2238
- Neun BW, Ilinskaya AN, Dobrovolskaia MA (2018) In Characterization of nanoparticles intended for drug delivery 91–102. Springer
- Nguyen VH, Lee BJ (2017) Protein corona: a new approach for nanomedicine design. *Int J Nanomedicine* 12:3137–3151
- Ojea-Jimenez I, Comenge J, Garcia-Fernandez L, Megson ZA, Casals E, Puentes VF (2013) Engineered inorganic nanoparticles for drug delivery applications. *Curr Drug Metab* 14:518–530
- Oshiro-Junior JA, Alves RC, Hanck-Silva G, Sato MR, Rodero C, Eloy JO, Chorilli M (2018) Stimuli-responsive drug delivery nanocarriers in the treatment of breast cancer. *Curr Med Chem*
- Panchapakesan B, Lu S, Sivakumar K, Taker K, Cesarone G, Wickstrom E (2005) Single-wall carbon nanotube nanobomb agents for killing breast cancer cells. *NanoBiotechnology* 1:133–139
- Peer D, Karp JM, Hong S, Farokhzad OC, Margalit R, Langer R (2007) Nanocarriers as an emerging platform for cancer therapy. *Nat Nanotechnol* 2:751
- Peetla C, Bhave R, Vijayaraghavalu S, Stine A, Kooijman E, Labhasetwar V (2010) Drug resistance in breast cancer cells: biophysical

- characterization of and doxorubicin interactions with membrane lipids. *Mol Pharm* 7:2334–2348
- Prasad PV, Purkayastha K, Sharma U, Barik M (2020) Ph-sensitive nanomedicine for treating gynaecological cancers. *J Woman's Reproduct Health* 2:35
- Qi S-S, Sun J-H, Yu H-H, Yu S-Q (2017) Co-delivery nanoparticles of anti-cancer drugs for improving chemotherapy efficacy. *Drug Deliv* 24:1909–1926
- Rivera E (2003) Current status of liposomal anthracycline therapy in metastatic breast cancer. *Clin Breast Cancer* 4:S76–S83
- Roszak J, Smok-Pieniżek A, Spryszyńska S, Kowalczyk K, Domeradzka-Gajda K, Świercz R, Grobelny J, Tomaszewska E, Ranoszek-Soliwoda K, Celichowski G, Cieślak M, Puchowicz D, Stępnik M (2020) Cytotoxic effects in transformed and non-transformed human breast cell lines after exposure to silver nanoparticles in combination with selected aluminium compounds, parabens or phthalates. *J Hazard Mater* 392:122442
- Rudzińska M, Parodi A, Soond SM, Vinarov AZ, Korolev DO, Morozov AO, Daglioglu C, Tutar Y, Zamyatnin AA (2019) The role of cysteine cathepsins in cancer progression and drug resistance. *Int J Mol Sci* 20:3602
- Rudzińska M, Daglioglu C, Savvateeva LV, Kaci FN, Antoine R, Zamyatnin AA Jr (2021) Current status and perspectives of protease inhibitors and their combination with nanosized drug delivery systems for targeted cancer therapy. *Drug Des Dev Ther* 15:9–20
- Senapati S, Mahanta AK, Kumar S, Maiti P (2018) Controlled drug delivery vehicles for cancer treatment and their performance. *Signal Transduct Target Ther* 3:1–19
- Shao N, Lu S, Wickstrom E, Panchapakesan B (2007) Integrated molecular targeting of IGF1R and HER2 surface receptors and destruction of breast cancer cells using single wall carbon nanotubes. *Nanotechnology* 18:315101
- Shi C, Guo D, Xiao K, Wang X, Wang L, Luo J (2015a) A drug-specific nanocarrier design for efficient anticancer therapy. *Nat Commun* 6:1–14
- Shi H, Li L, Zhang L, Wang T, Wang C, Zhu D, Su Z (2015b) Designed preparation of polyacrylic acid/calcium carbonate nanoparticles with high doxorubicin payload for liver cancer chemotherapy. *CrystEngComm* 17:4768–4773
- Shi J, Kantoff PW, Wooster R, Farokhzad OC (2017) Cancer nanomedicine: progress, challenges and opportunities. *Nat Rev Cancer* 17:20
- Singh R, Lillard JW Jr (2009) Nanoparticle-based targeted drug delivery. *Exp Mol Pathol* 86:215–223
- Takashimizu Y, Iiyoshi M (2016) New parameter of roundness R: circularity corrected by aspect ratio. *Prog Earth Planet Sci* 3:1–16
- Tang Y, Wang X, Li J, Nie Y, Liao G, Yu Y, Li C (2019) Overcoming the reticuloendothelial system barrier to drug delivery with a “don't-eat-us” strategy. *ACS Nano* 13:13015–13026
- Tian B, Wang Q, Su Q, Feng W, Li F (2017) In vivo biodistribution and toxicity assessment of triplet-triplet annihilation-based upconversion nanocapsules. *Biomaterials* 112:10–19
- Torchilin VP (2005) Recent advances with liposomes as pharmaceutical carriers. *Nat Rev Drug Discov* 4:145–160
- Ud Din F, Aman W, Ullah I, Qureshi OS, Mustapha O, Shafique S, Zeb A (2017) Effective use of nanocarriers as drug delivery systems for the treatment of selected tumors. *Int J Nanomed* 12:7291
- Ventola CL (2017) Progress in nanomedicine: approved and investigational nanodrugs. *Pharm Ther* 42:742
- Wang Y, Jiang L, Yin Q, Liu H, Liu G, Zhu G, Li B (2017) The targeted antitumor effects of C-PC/CMC-CD59sp nanoparticles on HeLa cells in vitro and in vivo. *J Cancer* 8:3001
- Warheit DB, Webb TR, Colvin VL, Reed KL, Sayes CM (2007) Pulmonary bioassay studies with nanoscale and fine-quartz particles in rats: toxicity is not dependent upon particle size but on surface characteristics. *Toxicol Sci* 95:270–280
- Wicki A, Witzigmann D, Balasubramanian V, Huwyler J (2015) Nanomedicine in cancer therapy: challenges, opportunities, and clinical applications. *J Control Release* 200:138–157
- Wu H, Zhu L, Torchilin VP (2013) pH-sensitive poly (histidine)-PEG/DSPE-PEG co-polymer micelles for cytosolic drug delivery. *Biomaterials* 34:1213–1222
- Xin Y, Yin M, Zhao L, Meng F, Luo L (2017) Recent progress on nanoparticle-based drug delivery systems for cancer therapy. *Cancer Biol Med* 14:228
- Xu X, Ho W, Zhang X, Bertrand N, Farokhzad O (2015) Cancer nanomedicine: from targeted delivery to combination therapy. *Trends Mol Med* 21:223–232
- Xu B, Yuan L, Hu Y, Xu Z, Qin J-J, Cheng X-D (2021) Synthesis, Characterization, Cellular Uptake, and In Vitro Anticancer Activity of Fullerene-Doxorubicin Conjugates. *Front Pharmacol* 11:1685
- Xue W-F, Hellewell AL, Hewitt EW, Radford SE (2010) Fibril fragmentation in amyloid assembly and cytotoxicity: when size matters. *Prion* 4:20–25
- Yue H, Wei W, Yue Z, Lv P, Wang L, Ma G, Su Z (2010) Particle size affects the cellular response in macrophages. *Eur J Pharm Sci* 41:650–657
- Zanganeh S, Spitler R, Erfanzadeh M, Alkilany AM, Mahmoudi M (2016) Protein corona: opportunities and challenges. *Int J Biochem Cell Biol* 75:143–147
- Zensi A, Begley D, Pontikis C, Legros C, Mihoreanu L, Wagner S, Büchel C, Von Briesen H, Kreuter JR (2009) Albumin nanoparticles targeted with Apo E enter the CNS by transcytosis and are delivered to neurones. *J Control Release* 137:78–86
- Zhivotovsky B, Gahm A, Orrenius S (1997) Two different proteases are involved in the proteolysis of lamin during apoptosis. *Biochem Biophys Res Commun* 233:96–101
- Zhou AL, Swaminathan SK, Curran GL, Poduslo JF, Lowe VJ, Li L, Kandimalla KK (2019) Apolipoprotein A-I crosses the blood-brain barrier through clathrin-independent and cholesterol-mediated endocytosis. *J Pharmacol Exp Ther* 369:481–488

Publisher's Note Springer Nature remains neutral with regard to jurisdictional claims in published maps and institutional affiliations.